Computational Modeling of Bio-Fluid Mechanics of White Blood Cells

by

Murat Bahadır Soydan

A Thesis Submitted to the
Graduate School of Engineering
in Partial Fulfillment of the Requirements for
the Degree of

Master of Science

in

Mechanical Engineering

Koç University

September, 2004

Koç University

Graduate School of Sciences and Engineering

This is to certify that I have examined this copy of a master's thesis by

Murat Bahadır Soydan

and have found that it is complete and satisfactory in all respects,
and that any and all revisions required by the final
examining committee have been made.

Committee Members:

Assistant Prof. Metin Muradoğlu (Advisor)

Assistant Prof. Çağatay Başdoğan

Prof. Sezai Saraç

Date: 14/09/2004

To my mother, father and sister

ABSTRACT

The white blood cell is a soft biomaterial that exhibits unique behavior when exposed to the action of a flowing fluid. This behavior often determines the structure-function relationships of the cell-fluid system and gives information on many important processes taking place in living systems. The equilibrium behavior of leukocytes in solvent is relatively well known, but their dynamics is not yet investigated extensively. In the present thesis, the cell is modeled as a viscous fluid that moves in a surrounding less viscous fluid. The dynamics of large-scale deformations of the leukocytes in a given flow field is investigated. In particular; the micro-pipette aspiration of leukocytes is analyzed; and the adhesion dynamics of leukocytes to ligand-coated surfaces is modeled and simulated within the framework of finite-difference/front-tracking methodology. The events such as attachment, detachment, and rolling of leukocytes in shear flow are analyzed. The nucleus of the white blood cell is modeled as a compound drop and uniformly distributed linear springs are used between the nucleus and the cortex to model the effects of the internal structures such as microtubles and microfilaments in the cytoplasm. The new model allows both co-centric and off-centric configurations of the nucleus and cortex; and it is fully reversible, i.e., the cell restores to its initial undeformed configuration when the external forces are removed.

Keywords: Cell Deformation, Micro-pipette aspiration, Cell Adhesion, Front-tracking.

ACKNOWLEDGMENTS

First and foremost, I would like to express my deepest gratitude to my advisor, Assistant Prof. Metin Muradoğlu for his supervision, support and time spent in all steps of the development of this thesis. I am proud of being one of his students who have been able to learn from his deep knowledge.

My special thanks go to my co-advisor Prof. Burak Erman, whose valuable comments made the initiation and development of this work possible.

I would like to thank Assistant Prof. Selman Nas for his great support during the middle phase of this study.

I am grateful to Assistant Prof. Çağatay Başdoğan and Prof. Sezai Saraç for their participation in my thesis committee and for the critical reading of my thesis.

I also would like to thank my all grad student friends at the Koç University, especially Harun, Doruk, Tuğrul, Erhan and Davut for the beautiful atmosphere they have created around me.

Finally, my sincere thanks go to my mother Hülya Soydan, my father Ahmet Bahattin Soydan and my sister Fulya Berrin Soydan for their love, support and patience throughout my whole life.

TABLE OF CONTENTS

LIST OF TABLES

LIST OF FIGURES

NOMENCLATURE

WBC	White blood cell
CFD	Computational fluid dynamics
PDE	Partial differential equation
$\mathbf{u}$	Velocity field
u	Horizontal component of the velocity
v	Vertical component of the velocity
p	Pressure
ρ	Density
μ	Viscosity
t	Time
$\mathbf{D}$	Rate of deformation tensor
κ	Curvature
$\mathbf{n}$	Normal vector to the interface
$\mathbf{x}_f$	Position of the interface
$\mathbf{f_b}$	Body forces
$\mathbf{g}$	Gravitational acceleration
L_p	Projection length
Re	Reynolds number
γ	Ratio of the inner spring to the surface tension forces
F_b	Total bond force
σ	Spring constant
σ_{ts}	Transition state spring constant
λ	Equilibrium bond length
y_m	Actual bond length
N_b	Bond density
k_r	Reverse reaction rate coefficient

k_f	Forward reaction rate coefficient
k_bT	Thermal energy (product of the Boltzmann constant and temperature)
N_{bo}	Initial bond density
k_{fo}	Equilibrium forward reaction rate
k_{ro}	Equilibrium reverse reaction rate
τ_r	Reference time scale
λ_r	Reference length scale
N_{br}	Reference bond density
t^*	Dimensionless time
N_b^*	Dimensionless bond density
y_m^*	Dimensionless distance between the receptor and the substrate's surface

Chapter 1

INTRODUCTION

Leukocytes or white blood cells (WBC) which are produced in the bone marrow involve in defending the body against ineffective organisms and foreign substances. They are the basic components of the immune system. There are five main types of WBC, subdivided between two main groups:

1. Polymorphonuclear Leukocytes (granulocytes)
   (a) Neutrophils
   (b) Eosinophils
   (c) Basophils
2. Mononuclear Leukocytes
   (a) Monocytes
   (b) Lymphocytes

The number of WBCs per mili liter blood is called WBC count which normally ranges from 4100/ml to 10900/ml. But this value can be changed considerably by factors such as exercise, stress and disease. A low WBC count may indicate viral infection or toxic reactions. A high WBC count may indicate infection, leukemia, or tissue damage [1]. Leukemia is one of the major types of cancer which is characterized by an abnormal increase in number of WBCs. Table 1.1 shows the normal percentage values of each type of white blood cell in a sample of blood of an adult human being.

Leukocytes can be observed in the circulation in a passive or an active state. In the passive state they deform only in response to an external applied stress, such as the plasma

Type of WBC	**Percentage**	**Number per mili liter of blood**
Neutrophil	50 - 60 %	3000 - 7000
Eosinphils	1 - 4 %	50 - 400
Basophils	0.5 - 2 %	25 - 100
Lymphocytes	20 - 40 %	1000 - 4000
Monocytes	2 - 9 %	100 - 600

Table 1.1: The normal percentage values of each type of white blood cell in a sample [1].

fluid stress, or adhesive stress to the endothelium whereas in the active state the cells deform spontaneously [3].

The neutrophil is the most common leukocyte in human blood. Neutrophils are spherical with a diameter of about 8 micrometer in a passive, non-reactive state. The membrane of the neutrophil is highly ruffled, giving it an excess surface area (estimated as 110% - 120% of the undeformed sphere) and permits deformation at constant volume. It contains a relatively small segmented nucleus, occupying about 21% of its volume, and a cytoplasm which is rich in granules (tiny grains). In contrast, in a lymphocyte, the nucleus occupies approximately 44% of the cell [4].

Leukocytes are larger and much stiffer than red blood cells (erythtocytes). Because of that their presence is critical to the fluid mechanics of blood flow in the peripheral blood vessels, where the vessel diameters are comparable to those of the cells. Leukocytes must deform to make their way through narrow micro-capillaries, and to fit between the endothelial cells lining the blood vessels in order to reach the sites of infection. Because the leukocyte is stiff and difficult to deform, it can plug micro-capillaries, leading to events such as ischemic stroke [5]. These circulating cells have been implicated in the blockage of capillaries when a blood vessel is ruptured [6]. In an attempt to understand and quantify the mechanical behavior of leukocytes, several experimental procedures and mathematical models have been developed. While these have provided many insights into the mechanical properties of leukocyte, there is still contention as to what the constitutive equation for the deformation should be.

Cell adhesion involves receptors, cells, and vessels with dimensions on the order of nanometer, micrometer, and centimeter, respectively. Multi-scale modeling of blood flow through arteries is significant for understanding the physiological functions of the circulatory system and the patho-physiology of disease processes such as hypertension and diabetes, as well as for the diagnosis and medical cure of certain cardiovascular diseases. The study of the effect of leukocyte adhesion on blood flow in micro-vessels is important for understanding the resistance changes in micro-circulation [7]. Previously proposed many models [8, 2] do not take into account the rheological properties (viscosity and surface tension) of the leukocyte. But today, these properties have been shown to have strong effect on the adhesion process [9].

The purpose of this work is to develop and implement a modular computational environment for the study of white blood cell deformation and adhesion.

What follows is a summary of the organization of this thesis. Chapter 2 provides a literature review on cell deformation and cell adhesion concerning about the leukocytes. In Chapter 3, the governing equations are reviewed and the finite-difference/front-tracking algorithm is described. Chapter 4 describes the incorporation of various representative models for the deformation of leukocytes into the basic numerical method, and the effects of different models on the outcome of cell-entry, micro-pipette simulations. Chapter 5 describes the micro- and macro-scale models, their integration in order to build a multi-scale model, the numerical integration of the kinetic equation, and a representative simulation on the detachment and rolling of leukocytes on the ligand-coated surfaces. Finally, the conclusions are presented in Chapter 6.

Chapter 2

LITERATURE REVIEW

2.1 Review on Cell Mechanics

Detailed experimental studies have been performed by many researchers in order to understand and quantify the physics of deformation and recovery of cells. It were observed that cells deform in response to external pressures and shear forces and that they recover their undeformed shape when the external forces are removed. These observations have led researchers to reason out that cells exhibit characterizable material behavior which means that their deformation can be described mathematically by relating material stresses to strains and strain rates, through appropriate viscous and elastic parameters. The use of micro-manipulation is a common experimental technique. Cell entry [3, 10] and cell expulsion [11] experiments commonly used this technique. In cell entry experiments, a cell is pulled by a micro-pipette at a constant suction pressure. With the help of the specialized video cameras the experiment is recorded and the distance from the leading edge of the cell to the entry of the micrometer is plotted as a function of time. Material properties of the cell such as viscosity and elasticity can be computed assuming a constitutive relationship between the stresses and the deformation of the cell, and using this relationship by evaluating the data collected by the experiment. In the cell expulsion experiments, the cell is completely inside the micro pipette, and it is expelled by applying a positive pressure difference. The expelled cell recovers its original shape with time. During its recovery, using video cameras the two main diameters of the cell are recorded as a function of time. A constitutive relationship between the stresses and the deformation of the cell must be assumed in order to interpret the collected data. As a result of these micromanipulation experiments the researchers concluded that different cells deform differently.

Theoretical and experimental study of leukocytes (predominantly the relatively abundant neutrophils and lymphocytes) to determine a suitable constitutive model has been a challenging area of research. Theoretical efforts at constitutive modeling of the leukocytes

have been interrupted by novel experiments that have periodically upset tentatively accepted models. Schmid-Schonbein et al. [3] assumed that the leukocyte behaved as a viscoelastic solid and accurately described small deformations of the neutrophils into a micro pipette. Yeung and Evans [12] modeled the leukocyte as a Newtonian liquid drop enclosed by a cortical layer of constant tension. Cytoplasmic viscosity and cortical tension were the main parameters of the leukocyte model. Their model were able to describe large deformations of leukocyte into a micro-pipette. However, Yeung and Evans' model failed to simulate the behavior of the leukocyte at small deformations, whereas the model by Schmid-Sconbein et al. [3] failed at large deformations.

The inner structure of the leukocyte is embedded with a network of filamentous macromolecules [13]. Needham et al. [13] performed micro-pipette experiments, as a result of their observations they suggested that the rheological properties of the cell depend on deformation extent and on deformation rate and that the cell exhibited non-Newtonian behavior during its deformation and recovery. The non-Newtonian response is suggested as the result of extension and unwinding of the filamentous network [14]. In an attempt to include non-Newtonian effects in the leukocyte model, Tsai et al. [15] used a power law shear-thinning (the viscosity decreases as the shear rate increases) model for the cytoplasmic viscosity and they assumed that the cortical tension of the leukocyte was constant. Their model was able to simulate a large part of the shear-rate dependency of the viscosity of the leukocyte in the aspiration phase, but it failed to predict the rapid elastic response in the initial entry of the leukocyte into the micro-pipette.

Dong and Skalak [16] proposed a finite-element model using a Maxwell fluid for the cytoplasm and a strain-dependent cortical tension. Their model could predict the behavior of the leukocyte both for small and large deformations only if the material properties were varied continuously during deformation of the leukocyte. Thus, the Maxwell model is not a sufficient constitutive model for the leukocyte.

Dong et al. [16, 17] and Bottino [14] have modeled the cortical layer of the cell as an elastic membrane which had a nonlinear stress-strain response. The membrane of the leukocyte is composed of folds, which causes excess surface area. Thus, during large deformations the membrane of the cell exhibits low resistance to area extension until it is unfolded. When the membrane is completely unfolded, the resistance to further stretching increases steeply.

Dong et al. [16, 17] and Bottino [14] have not explored the full range of deformation and recovery using this model and the effect of this cortical model on leukocyte rheology has not been completely clarified.

Bottino [14] modeled the internal structure of the leukocyte as a network of interconnected elastic links. The forces developed within the links were transmitted through body forces to the underlying viscous fluid using the immersed boundary technique. He adopted various models for the stress-strain relationships in the interconnected network. In his model, the range of deformation studied was limited and it is not clear how experimental measurements of leukocyte properties can be directly correlated with the properties of the modeled elastic network.

Drury and Dembo [18, 19] proposed a model in order to capture the "jumps" in the aspiration rates of leukocytes in micro-pipette aspiration experiments. Such jumps occur in the initial phase of aspiration and toward the end of the aspiration process as the entire cell enters the pipette. In the bulk of the aspiration process the entry rate of the cell is nearly uniform. In order to simulate this behavior they modeled the cortex and cytoplasm of the cell with shear-thinning property. Their model supplied reasonable behavior with respect to the dependency of aspiration time scale on aspiration pressures and pipette radius. However, the model did not completely predict the response of the cell, especially with respect to the initial jump of the cell into the pipette.

Dong et al. [17] and Hochmuth [13] suggested that the elastic recoil followed by slow recovery upon expulsion of leukocytes from micro-pipettes suggested a dual-time scale response that arose from a multilayer internal structure of the leukocyte. They modeled the leukocyte as a compound drop, this is, they incorporated the nucleus to the leukocyte model as a fluid which is more viscous than the cytoplasm and the ambient fluid. The tension of the nucleus was assumed to be constant and the cytoplasm and nucleus was modeled as Newtonian-fluid. It was argued that the dual time-scale response arose because, during recovery, the less viscous cytoplasm would recover rapidly, followed by a slower recovery phase at which the nucleus recovered to its original shape. This model could not simulate the rapid elastic response seen in experiments. Thus, the compound-drop model did not exhibit deformation-rate dependent effects as demonstrated by shear thinning fluids. Shy et al. [20] added elastic and shear-thinning aspects to the compound-drop model in

order to investigate whether such elements can predict the full range of leukocyte behavior. Their model did not capture the full range of leukocyte behavior observed in micro-pipette experiments.

Udaykumar et al. [5] proposed a compound cell model which is composed of the membrane cortex, cytoplasm and nucleus. They modeled the cortical layer as an elastic membrane with a nonlinear stress-strain curve to simulate unfolding of the excess surface area of the membrane. They used a power-law shear thinning fluid for the cytoplasm. The nucleus was treated as a Newtonian fluid and the tension of the nucleus membrane was assumed to be constant. They concluded that the compound cell model with elastic membrane approaches most closely the leukocyte responses observed in some experiments. However, their shear-thinning viscosity model failed to capture the experimentally observed shear-rate response of the leukocytes.

Ingber [21, 22] proposed a mechanical model of cell structure based on tensegrity (tensional integrity) architecture that explains how the mechanical behavior of the cell emerges from physical interactions among the different molecular filament systems that form the cytoskeleton. The cytoskeleton is a three-dimensional structure that fills the cytoplasm. This structure acts as both muscle and skeleton, and is responsible for the cell movement and stability. The primary types of fibers comprising the cytoskeleton are microfilaments, microtubles, and intermediate filaments. Cytoskeletal filaments both generate and resist mechanical loads, and they are largely responsible for the cells ability to resist shape distortion. Ingber's model predict many aspects of cell behavior, but it should be improved in order to account for a detailed model of a particular cell type.

2.2 Review on Cell Adhesion

Adhesion of cell receptors and surface ligands under flow conditions starts by migration of the cell from the blood stream toward the vessel surface. This may be followed by primary adhesion, rolling or permanent adhesion. These processes are essential events in physiological adhesion such as leukocyte accumulation during inflammation, tumor cell metastasis (the spreading of the disease to another cells) and thrombus formation [23].

Adhesion to vascular endothelium is mediated by a series of different endothelial cell-leukocyte adhesion molecules. Selectins, integrins and immunoglobins are the three basic

classes of leukocyte-endothelium adhesion molecules [24] which are membrane proteins. Detailed experimental studies of the adhesive bonds have suggested that adhesion molecules of the selectin family are involved in maintaining the initial rolling of the leukocytes on the endothelium, whereas the integrin bonds are responsible for firm adhesion of leukocytes to the endothelium [25].

Many mathematical models have been proposed in order to describe different events which are significant in cell adhesion. These models can be divided into two main classes based on equilibrium and kinetics concept. Bell et al. [26] developed an equilibrium model and proposed that adhesion is a competition between the specific binding of surface molecules, and the non-specific repulsion between the cells caused by the presence of charges and long polymers in the cell surfaces. An important concept developed by this model is the assumption that molecular bonds behave as springs, and that the equilibrium association constant between molecular bonds must be a function of the distance between the membranes. The usefulness of this model is limited because actually adhesion is a dynamic process which might not reach equilibrium.

Evans [27, 28] proposed an equilibrium model in which he developed a relationship between the mechanical properties of the cell membrane and two types of bonds: immobile discrete bonds, and a continuous adhesive film. He described a piece of membrane adhered to a planar surface. The piece of membrane was efficiently constrained at one end and lifted away from the surface at the other end by a constant applied tension. An important conclusion of this model was that discrete bonds could account for the large detachment forces observed experimentally (larger than the forces required to form the adhesive contact). The main limitations of this model were the equilibrium assumption and the consideration of only a portion of the cell membrane.

Since adhesion is a dynamic process, the kinetics approach is more capable of handling the dynamics of cell adhesion and rolling. In this approach, formation and dissociation of bonds occur according to the reverse and forward reaction rate constant. Using this concept, Hammer and Lauffenburger [29] studied the effects of external flow on cell adhesion. The cell was modeled as a solid sphere, and the receptors at the surface of the sphere were assumed to diffuse and into the contact area. They related the permissible shear stress (the maximum shear stress that leaves the cell attached) to the total number of receptors on the cell, and

to their diffusion coefficient. Although the model of Hammer and Lauffenburger [29] was the first to incorporate the effects of external flow in a model of cell adhesion, they failed to account for the deformation of the cell.

Dembo et al. [2] developed a kinetic model based on the ideas of Evans [27, 28] and Bell [26]. In this model, a piece of membrane was attached to the wall, and a pulling force was exerted on one end while the other end was held fixed. They modeled the cell membrane as a thin inextensible membrane. They allowed the membrane to detach by letting the applied tension exceed the bond stress. The kinetics for bond formation and rupture were modeled by deriving kinetic rate constants from Bells' [26] expression for the equilibrium dissociation constant. Dembo et al. [2] used their model to predict the critical membrane tension required for detachment, and the resulting peeling velocities of the membrane. The main contribution of this model was the expression for the rate constants as a function of distance between membranes. The main limitations were the assumption that the bonds were mobile, and that only the deformation of a portion of the membrane was considered.

The model of Dembo et al. [2] was extended using a probabilistic approach for the very initial formation of bonds by Cozens-Roberts et al. [30]. Other authors who used the probabilistic approach and Monte Carlo simulation to study the adhesion process are as reviewed by Zhu [31]. Dembo's model has also been extended to account for the distribution of microvilli on the surface of the cell and to simulate the rolling and the adhesion of a cell on a surface under shear flow. Hammer and Apte [32] modeled the cell as a micro-villi-coated hard sphere covered with adhesive springs. The binding and breakage of bonds and the distribution of the receptors on the tips of micro-villi were computed using a probabilistic approach. Hammer and Apte [32] studied the effects of the number of receptors, density of ligands, rates of reaction between receptor and ligand, and stiffness of the receptor-ligand spring on the adhesion of the cell. Several models have been presented which included minor modifications of these previous models, but none of them considered the cell deformability, which has been shown to be necessary for calculating the magnitude of the adhesion force. Dong et al. [33] and Dong and Lei [9] have modeled the cell as a liquid drop enclosed by an elastic ring. They showed how the deformability and the adhesion parameters affect the adhesion process between leukocyte and endothelium in shear flow. The main limitation of their model was that only a small portion of the adhesion length is allowed to peel away

from the vessel wall.

N'dri [7] and N'dri et al. [34] have used a multi-scale computational approach [34] for studying the adhesion kinetics and the deformation and movement of a cell on a substrate. In this multi-scale model, the macroscopic component took care of the deformation of the cell at the continuum level, and the microscopic part dealt with the adhesion and the deformation of the bonds using the kinetics model. At the receptor-ligand level, they used the kinetic model proposed by Dembo [2] in which a bond molecule was mechanically represented by a spring and a reversible kinetics approach was used to describe the association and dissociation of bonds. In their macro-scale model, communication between the macro- and micro-scale models was performed interactively with iterations between models until both levels approach well-matched solution in each time step. The computational model was tested using a cell adhering and deforming along the vessel wall under imposed shear flows. The results were consistent with existing numerical and experimental results. The main findings of this model were that the presence of the nucleus (when the cell is modeled as a compound drop) increased the bond lifetime and that increasing cell surface tension decreased the bond lifetime. Furthermore, it is found that increasing cell viscosity for a fixed hydrodynamic force increased linearly the critical bond force (the minimal amount of force necessary to rupture the bond), whereas decreasing cell surface tension inversely decreased it. Although this multi-scale model [7, 34] have combined the macro- and micro scale levels of the adhesion and movement of cell on a substratum effectively, its continuum model needs to be improved in order to demonstrate the effect of the deformation of the cell on the adhesion process more comprehensively.

Chapter 3

COMPUTATIONAL FRAMEWORK

This chapter describes the fundamental numerical framework for the remainder of this thesis. The cells in this thesis have been modeled as one or various Newtonian fluid bodies deforming arbitrarily in another Newtonian fluid. These fluid bodies are enclosed by massless membranes, and their deformation occurs in response to either a surface force applied on the membrane, or the forces exerted on them by the motion of the surrounding fluid. The flexibility in the mechanical model for the cells used in thesis have been achieved in a way that the parameters of the Newtonian fluids (the density and viscosity) could be modified and the mechanical properties of the massless membranes could be altered. Furthermore, the membranes were treated independently in a separate module and interacted with fluids through an external force term. The bulk mechanical behavior of the cell could be modified by adding one or more internal bodies. These bodies could represent the nucleus or other organelles inside the cell and would be constructed using the same elements just described: a different fluid enclosed by a massless membrane.

The methodology described in this chapter consists of using Computational Fluid Dynamics (CFD) techniques to develop a numerical method to solve the mathematical representation of the physical model described above. This chapter begins with a display of the governing equations that describe the behavior of incompressible, Newtonian fluids with surface forces. The second section presents the details of the numerical method used to solve the governing equations and summarizes the overall solution procedure.

3.1 Governing Equations

The problem of leukocyte deformation, adhesion and movement is solved using the Navier-Stokes equations. These equations are written for the whole flow field and different phases are treated with variable material properties. The effects of surface forces are modeled as body forces and are included in the momentum equations as δ-functions at the phase

boundaries [35]. In the Cartesian coordinates, two dimensional time dependent Navier-Stokes equations for incompressible flow can be written in conservative form as follows:

$$\frac{\partial}{\partial t}(\rho \mathbf{u}) + \nabla \cdot (\rho \mathbf{u}\mathbf{u}) = -\nabla p + \rho \mathbf{g} + \nabla \cdot (2\mu \mathbf{D}) + \sigma \kappa \mathbf{n} \delta(\mathbf{x} - \mathbf{x}^f) + \mathbf{f_b}, \tag{3.1}$$

where $\mathbf{u}$ is the velocity field; ρ and μ are the discontinuous density and viscosity fields, respectively. $\mathbf{D}$ is the rate of deformation tensor, whose components are $D_{ij} = \frac{1}{2}\left(\frac{\partial u_i}{\partial x_j} + \frac{\partial u_j}{\partial x_i}\right)$. The fourth term in the right hand side of Eq.(3.1) represents the body forces resulting from the surface tension. Here σ is the surface tension coefficient, κ is the mean curvature, and $\mathbf{n}$ is a normal vector to the interface separating the two fluids. $\delta(\mathbf{x} - \mathbf{x}_f)$ is a delta function that is zero everywhere except at the interface, where $\mathbf{x} = \mathbf{x}_f$ ($\mathbf{x}_f$ denotes the position of the interface). The last term represents other body forces such as the forces due to springs between the cortex and the nucleus and the force due to cell adhesion; $\mathbf{g}$ is the gravitational acceleration. In this thesis gravitational acceleration is not considered, and is set to zero.

In order to solve Eq.(3.1) additional equations are needed which are the continuity equation representing the incompressibility condition

$$\nabla \cdot \mathbf{u} = 0, \tag{3.2}$$

and equations of state for the density and viscosity given by

$$\frac{\partial \rho}{\partial t} + \mathbf{u} \cdot \nabla \rho = 0, \quad \frac{\partial \mu}{\partial t} + \mathbf{u} \cdot \nabla \mu = 0, \tag{3.3}$$

which state that the density and viscosity of a fluid particle remain constant. In any case, in the method described in the following section, Eqs.(3.3) are not solved directly, but the fluid properties constructed from the tracked interface.

Boundary Conditions

The interfacial conditions adopted in the model are based on the mass conservation and force balances. The mass conservation at the interface is given by

$$\mathbf{u_{interface}} = (\mathbf{u} \cdot \mathbf{n})_1 = (\mathbf{u} \cdot \mathbf{n})_2, \tag{3.4}$$

where $\mathbf{u_{interface}}$ represents the interfacial velocity field; and the subscripts 1 and 2 represent the fluid outside and inside the cell, respectively.

In the absence of the body force $\mathbf{f_b}$ in Eq.(3.1), the balance of normal stresses (the dynamic Young-Laplace equation) is given as

$$p_2 - p_1 = \sigma\kappa + \mu_2(\frac{\partial u_n}{\partial n})_2 - \mu_1(\frac{\partial u_n}{\partial n})_1, \tag{3.5}$$

where κ is the curvature for two-dimensional flows, σ is the interfacial tension, $\mathbf{n}$ is the normal vector at the interface, and u_n is the component of the velocity vector in the direction of the normal vector $\mathbf{n}$.

3.2 Numerical Method

The finite-difference/front-tracking methodology developed by Unverdi and Tryggvason [35] is used in the present work. The Navier-Stokes equations are solved on a fixed, regular, staggered grid and the momentum equations (Eq.(3.1)) are discretized using a second-order central difference scheme for the spatial derivatives and an explicit predictor-corrector, second order projection time-integration scheme. A multi-grid method is used to solve the Poisson equation for the pressure.

3.2.1 Staggered Grid Arrangement

In order to approximate the solution to a set of PDEs (partial differential equations) one has to choose a discrete representation of the solution and the set of PDEs. In the finite difference approach one selects points in the computational domain where the unknowns are defined. Computational domains also called grids, can be categorized in many ways. The way the variables are arranged within each cell may be used to classify grids. A significant class of variable arrangement depends on the relative location of the unknowns in a problem, for example, the horizontal component of the velocity u, the vertical component of the velocity v and the pressure p in the incompressible Navier Stokes equations. In Fig. 3.1 collocated and staggered variable arrangements are illustrated. When u, v and p are located on the same node, the variables are said to be collocated. As an alternative, if the location of p is different from that of the velocities, the grid is called staggered. Staggered meshes were originally developed by Harlow and Welch [36] whose motivation was to avoid the decoupling of the pressure and the velocities in their discretized version of the Navier-Stokes equations. This decoupling occurs because the pressure at one node does not depend on the velocities at the

same node and vice-versa. It is seen in many common discretization of the incompressible Navier-Stokes equations, and it causes instabilities which result in spurious oscillations in the pressure field or even in a lack of convergence of the solution. Staggered meshes produce a natural coupling of the unknowns and have been successfully used by many researchers to solve the incompressible Navier-Stokes equations [37]. In this thesis, the Navier-Stokes equations are solved on a fixed, regular, staggered grid.

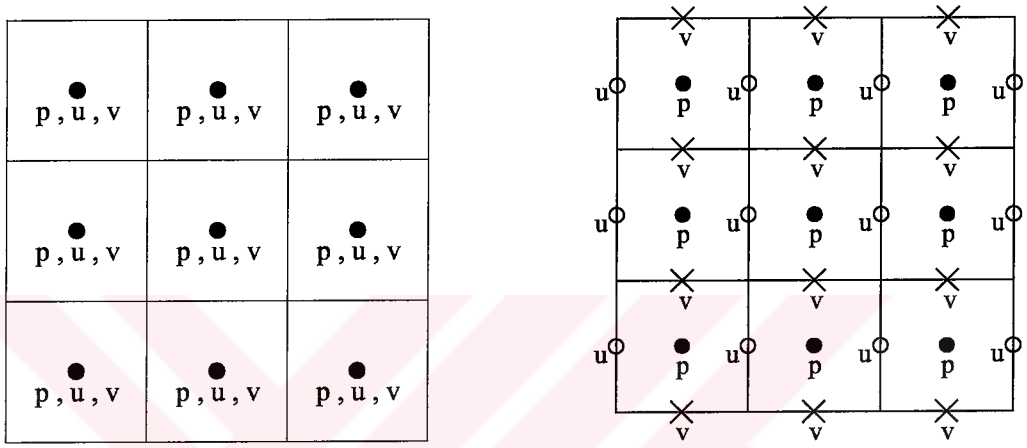

Figure 3.1: Collocated and staggered variable arrangements: a) in collocated grids all unknowns are located on the same node (depicted as the cell centroid in this figure); b) a staggered grid with the pressure node at the cell centroid, and the nodes for the components of the velocity at the center of the faces.

3.2.2 Integration of the Flow Equations

Equation (3.1) can be written as

$$\frac{\partial}{\partial t}(\rho \mathbf{u}) = \mathbf{A} - \nabla \mathbf{p}, \tag{3.6}$$

where

$$\mathbf{A} = -\nabla \cdot (\rho \mathbf{u}\mathbf{u}) + \rho \mathbf{g} + \nabla \cdot (2\mu \mathbf{D}) + \sigma \kappa \mathbf{n} \delta(\mathbf{x} - \mathbf{x}_f). \tag{3.7}$$

The discretization of Eq. (3.6) in time can be written as

$$\frac{\rho^{n+1}\mathbf{u}^{n+1} - \rho^n \mathbf{u}^n}{\Delta t} = \mathbf{A}_h^n - (\nabla_h p)^n, \tag{3.8}$$

where n denotes the time level; and the subscript h indicates the discrete versions of respective operators.

The discretized continuity equation in the new time level is given by

$$\nabla_h \cdot \mathbf{u}^{n+1} = 0. \tag{3.9}$$

In order to make use of the projection method Eq. (3.8) is splitted into two parts:

$$\frac{\rho^{n+1}\tilde{\mathbf{u}} - \rho^n \mathbf{u}^n}{\Delta t} = \mathbf{A}_h^n \tag{3.10}$$

$$\frac{\rho^{n+1}\mathbf{u}^{n+1} - \rho^{n+1}\tilde{\mathbf{u}}}{\Delta t} = -\nabla_h p \tag{3.11}$$

where $\tilde{\mathbf{u}}$ is the unprojected velocity field; n and $n+1$ are the current and new time steps, respectively.

The projection method involves three steps:

Step 1: Equation (3.10) is rearranged in order to separate the unprojected velocity field $\tilde{\mathbf{u}}$ from the entire equation as given by

$$\tilde{\mathbf{u}} = \frac{1}{\rho^{n+1}}(\rho^n \mathbf{u}^n + \Delta t \mathbf{A}_h^n). \tag{3.12}$$

In this step, Eq.(3.8) is solved without the pressure term to obtain the unprojected velocity field $\tilde{\mathbf{u}}$. It should be noted that $\tilde{\mathbf{u}}$ does not satisfy the continuity equation (Eq.(3.9)) at the new time level.

Step 2: Equation (3.11) is rearranged so that

$$\mathbf{u}^{n+1} - \tilde{\mathbf{u}} = -\Delta t \frac{1}{\rho^{n+1}} \nabla_h p. \tag{3.13}$$

Taking the divergence of Eq.(3.13) yields

$$\nabla_h \cdot \mathbf{u}^{n+1} - \nabla_h \cdot \tilde{\mathbf{u}} = -\Delta t \nabla_h \cdot (\frac{1}{\rho^{n+1}} \nabla_h p). \tag{3.14}$$

Since the continuity equation (Eq.(3.8)) must be satisfied at the new time level, Eq.(3.14) can be further simplified and rearranged as

$$\nabla_h \cdot (\frac{1}{\rho^{n+1}} \nabla_h p) = \frac{1}{\Delta t} \nabla_h \cdot \tilde{\mathbf{u}}. \tag{3.15}$$

Equation (3.15) is a Poisson type equation and is solved for the pressure.

Step 3: Equation (3.11) is rearranged in order to compute the velocity field $\mathbf{u}^{n+1}$ at the new time level as

$$\mathbf{u}^{n+1} = \tilde{\mathbf{u}} - \frac{\Delta t}{\rho^{n+1}} \nabla_h p. \tag{3.16}$$

The projected (corrected) velocity field $\mathbf{u}^{n+1}$ is computed using Eq.(3.16). In other words, the velocity field is corrected by projecting the divergence of pressure so that it satisfies the continuity equation (Eq.(3.9)).

The projection method is explicit and there are some constraints on the size of the time step due to the stability. An approximate linear stability analysis [38] shows that the constraint on the time step due to the convective terms in the momentum equation is

$$\Delta t \leq \frac{h}{|u_{max}|}, \tag{3.17}$$

the constraint due to the viscous term is

$$\Delta t \leq \frac{h^2}{4} \frac{\rho}{\mu}, \tag{3.18}$$

and the constraint due to the surface tension is

$$\Delta t \leq \sqrt{\frac{2\rho h^3}{4\pi\sigma\kappa_{max}}}, \tag{3.19}$$

where u_{max} is the magnitude of the maximum velocity of the fluid, h is the uniform grid size, Δt is the time step size, σ is the surface tension coefficient, κ_{max} is the maximum value of the curvature, ρ and μ are the density and the viscosity of the fluid, respectively. In the cases where there are multiple fluids, the minimum density/viscosity ratio is used for the viscous constraint.

3.2.3 Front Tracking Methodology

The front-tracking method developed by Unverdi and Tryggvason [35] is followed in this thesis. The interface between different phases are represented by a Lagrangian grid with connected marker points as shown in Fig. 3.2. The marker points which are connected with elements can be considered as massless fluid particles moving with local fluid velocity. Data structures such as linked lists are used to store both the points and the elements. The connectivity between the points and the elements is established through pointers which

contain information about the previous element and the next element in the list. The data stored in the list has an arbitrary order. The advantage of using a linked list is that it makes the addition and deletion of objects particularly simple. The key variables that are stored for a two-dimensional front are shown in Fig. 3.3. The point coordinates are the only information that are stored for each point, whereas most of the information are stored by the elements of the front. Each element contains information about the points, the elements that are connected to the same end points, the surface tension, the jump in density across the element, and any other quantities that are needed for a particular simulation.

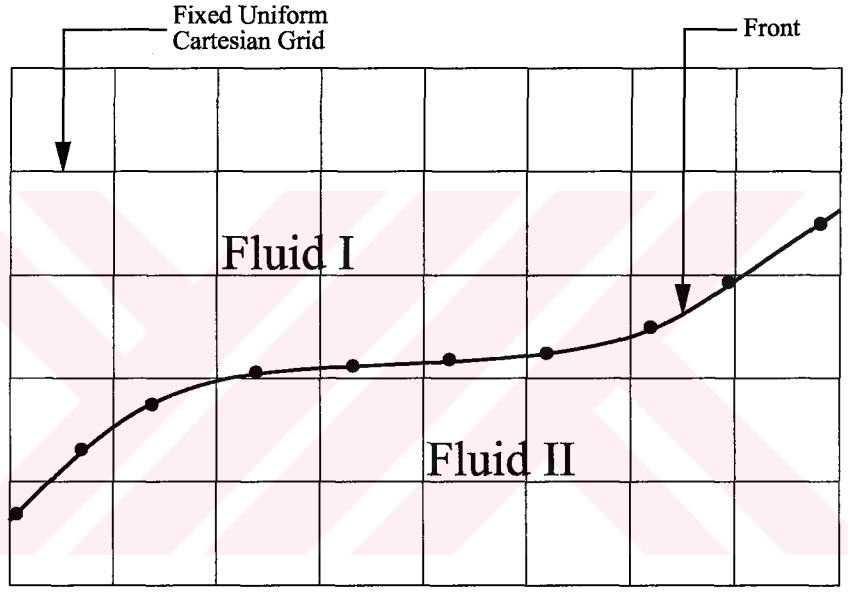

Figure 3.2: Computations of multiphase flows. The governing equations are solved on a fixed Eulerian grid and the interface (front) between different phases is represented by a Lagrangian grid consisting of connected marker points.

As the interface deforms, some marker points may come very close to each other, and other marker points may be far away from each other. An adequate resolution is maintained by adding computational elements as the interface stretches and by removing elements which become very small. This modification is done in a way that the distance between two markers is kept within a lower bound and an upper bound by adding and deleting points.

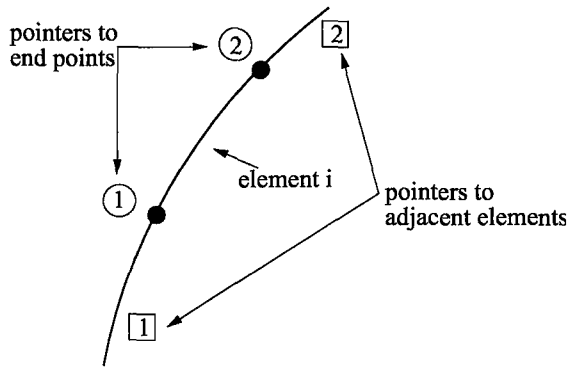

Figure 3.3: Structure of the two-dimensional front. Points and elements are stored in a linked list. Only the coordinates are stored for the points, but elements have pointers to the points and the adjacent elements.

Computation of Material Properties

One of the most significant parts of the Front-tracking method [35] is the way ρ and μ are updated. These variables are both discontinuous across the interface; therefore, it may occur either excessive numerical diffusion (error accumulation) or oscillations around the jump unless a special treatment is used at the front. In order to avoid these problems an additional computational element (the interface grid) that explicitly marks the position of the interface is used. The position of the interface is used to construct an indicator function, $\mathbf{I}(\mathbf{x})$, that is 1 inside the drop and 0 in the outer fluid. Figure. 3.4 represents the transition from one medium to another using the indicator function. Since ρ and μ are constant within each fluid, this indicator function allows the evaluation of the proper values of these variables at each grid point by

$$\begin{aligned} \rho(\mathbf{x}) &= \rho_o + (\rho_i - \rho_o)\mathbf{I}(\mathbf{x}), \\ \mu(\mathbf{x}) &= \mu_o + (\mu_i - \mu_o)\mathbf{I}(\mathbf{x}), \end{aligned} \tag{3.20}$$

where the subscripts o and i represent outer and inner fluid, respectively.

The sudden change of the density and viscosity from one grid point to next grid point may introduce disturbances of length scale equal to the mesh. In order to prevent this situation to occur, the interface is not kept completely sharp but given a small thickness of the order of the mesh size. In this transition area (see Fig. 3.4) the fluid properties

change smoothly from the value outside the front to the value inside the front. Since this artificial interface thickness is a function of the mesh size used only, and does not alter during the computations, no numerical diffusion is introduced. This finite thickness also helps to determine the position of the interface more accurately on the grid. If the indicator function were taken only the values 0 and 1, then it is only possible to express that the interface lies somewhere between grid points with different values. When the interface has a finite thickness which is larger than the mesh size, it is possible to determine its position exactly. Hence, when a jump is introduced on a stationary, discrete grid, it is not possible to specify an exact location and zero thickness simultaneously.

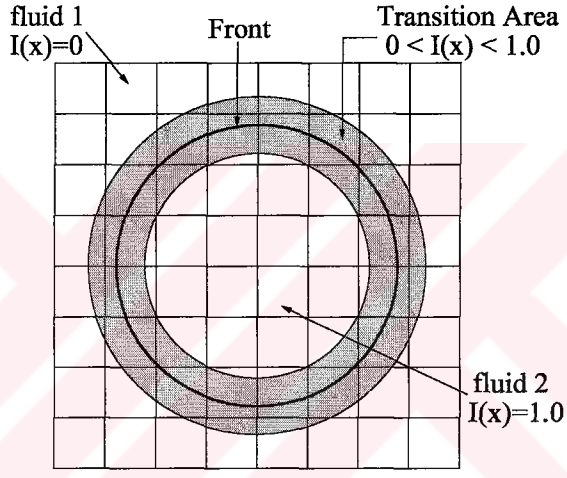

Figure 3.4: Transition from one medium to another using Indicator function.

Unverdi and Tryggvason [35] developed a fast property construction method. The basic elements of this method are as follows:

1. The jump in the indicator function transported by the interface is distributed to the grid points which lie close to the interface. This builds a grid-gradient field which has a finite thickness and is zero, except near the interface. The gradient of the indicator function evaluated at a stationary grid point $\mathbf{x}$ is denoted as $\mathbf{G}(\mathbf{x})$ and given as

$$\mathbf{G}(\mathbf{x}) = \sum_{l} D(\mathbf{x} - \mathbf{x}_{(l)})\mathbf{n}_l \Delta s_{(l)}, \tag{3.21}$$

where D is a "distribution function" that determines what fraction of the interface

quantity should go to each grid point, $\mathbf{n}_{(l)}$ is the unit normal vector to an interface element of line segment $\Delta s_{(l)}$ whose centroid is at $\mathbf{x}_{(l)}$.

2. The divergence of the gradient field ($\nabla_h \cdot \mathbf{G}$) is computed using second-order central differences. This quantity is zero in the entire computational domain, except near the interfaces.

3. The indicator function in the entire computational domain is computed by solving

$$\nabla_h^2 I = \nabla_h \cdot \mathbf{G}, \tag{3.22}$$

by a fast Poisson solver with the proper boundary conditions. In Eq.(3.22), the right-hand side is calculated in the previous steps 1 and 2. The Laplacian is discretized by the standard second-order, finite difference approximation.

The indicator function $I(\mathbf{x})$ is a field quantity, which is constant within each fluid, but has a finite thickness transition area around the interface.

In the calculations in this thesis, the distribution function

$$D(\mathbf{x}-\mathbf{x}^{(l)}) = \begin{cases} (4h)^{-\alpha} \prod_{i=1}^{\alpha} [1 + \cos \frac{\pi}{2h}(x_i - x_{(l)i})] & \text{if} \quad |x_i - x_{(l)i}| < 2h, \quad i = 1, \alpha \\ 0 & \text{otherwise,} \end{cases} \tag{3.23}$$

introduced by Peskin [39] is used. Here h is the Eulerian mesh width and $\alpha = 2$ (for two-dimensions).

Surface Tension

Following the procedure described by Unverdi and Tryggvason [35] the magnitude of the surface tension force is computed from the curvature of the interface:

$$\mathbf{f}_{(l)} = \sigma \kappa_{(l)} \mathbf{n}_{(l)} \Delta s_{(l)}. \tag{3.24}$$

Here σ is the surface tension coefficient, and $\kappa_{(l)}$ is the curvature of the interface at the centroid of element (l). This force is then distributed onto the grid in the same way as the gradient as shown in Fig. 3.5, thus constructing a grid-force field

$$\mathbf{F}(\mathbf{x}) = \sum_l D(\mathbf{x} - \mathbf{x}_{(l)}) \mathbf{f}_{(l)}. \tag{3.25}$$

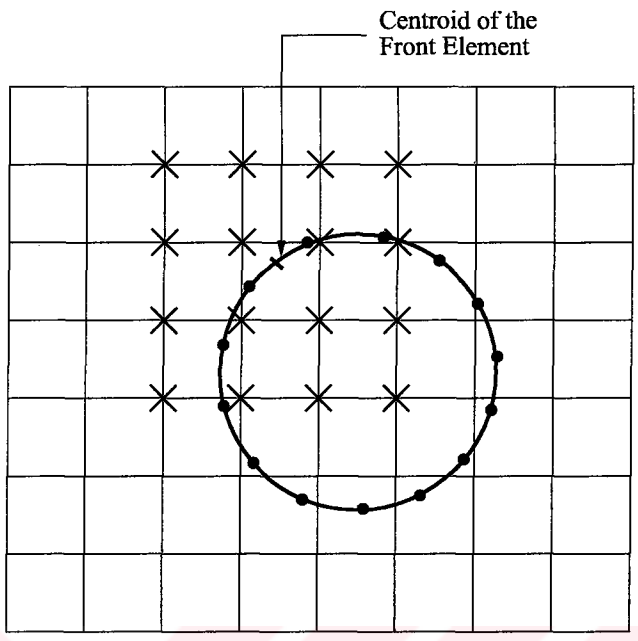

Figure 3.5: The weighted distribution of the surface tension force stored at the centroid of the front element to the 16 grid points which are located close to the centroid of the corresponding front element.

This guarantees that the total force is conserved during the transport from the interface to the grid. The distributed surface tension force is added as a body-force-like term into the equations of motion, and this term is involved in computation of the velocity field.

For the calculation of the curvature, a local, cubic polynomial is fitted to four points on the interface and the curvature is computed by differentiation with respect to the arc length. The surface tension force is found by evaluating the curvature at the middle of the element.

Interfacial Velocity Computation

By the interpolation of the velocities of the interface points from the grid velocities, the same grid points that the gradient was distributed to and the same weight functions are used. The velocity at interface point l is, therefore,

$$\mathbf{u}_{(l)} = \sum_i D(\mathbf{x} - \mathbf{x}_{(l)})\mathbf{u}_{(i)}, \tag{3.26}$$

where the sum is over the points on the stationary grid in the vicinity of the interface point. The interface is then advected by integrating

$$\frac{d\mathbf{x}_{(l)}}{dt} = \mathbf{u}_{(l)}. \tag{3.27}$$

3.2.4 The Overall Solution Procedure

The finite-difference MAC method and the front-tracking method are combined as follows. In advancing solutions from time level n ($t_n = n \cdot \Delta t$) to level $n+1$, a two-stage algorithm is used. The first stage yields first order accurate integration in time while the combination of the first and second stages yields a second order accuracy in time. In the first stage, the velocity vectors at the locations of the marker points are determined using the interpolations described in the previous section, for example, at marker point P,

$$\mathbf{u}^n_{(p)} = \mathbf{u}(\mathbf{x}^n_{(p)}). \tag{3.28}$$

Then the positions of the marker points are advanced using a first order Euler method

$$\widetilde{\mathbf{x}}^{n+1}_{(p)} = \mathbf{x}^n_{(p)} + \Delta t \mathbf{u}^n_{(p)} \tag{3.29}$$

and based on the new front position $\widetilde{\mathbf{x}}^{n+1}_{(p)}$, the material properties and surface tension forces are computed, i.e,

$$\rho^{n+1} = \rho(\widetilde{\mathbf{x}}^{n+1}_{(p)}); \quad \mu^{n+1} = \mu(\widetilde{\mathbf{x}}^{n+1}_{(p)}); \quad \mathbf{F}^{n+1} = \mathbf{F}(\widetilde{\mathbf{x}}^{n+1}_{(p)}). \tag{3.30}$$

Then the flow equations are solved using the MAC method to obtain the velocity and pressure fields $\widetilde{\mathbf{u}}^{n+1}$ and $\widetilde{\mathbf{p}}^{n+1}$, respectively. In the case of first order accurate scheme, the values at new time level are set to

$$\mathbf{x}^{n+1}_{(p)} = \widetilde{\mathbf{x}}^{n+1}_{(p)}; \quad \mathbf{u}^{n+1} = \widetilde{\mathbf{u}}^{n+1}; \quad \mathbf{p}^{n+1} = \widetilde{\mathbf{p}}^{n+1}; \quad \mu^{n+1} = \widetilde{\mu}^{n+1}; \quad \rho^{n+1} = \widetilde{\rho}^{n+1}. \tag{3.31}$$

To obtain a second order accuracy in time, the above procedure is repeated once again, i.e, the velocity field is first interpolated on the marker points to obtain

$$\widetilde{\mathbf{u}}^{n+1}_{(p)} = \mathbf{u}(\widetilde{\mathbf{x}}^{n+1}_{(p)}). \tag{3.32}$$

Then marker points are moved using an explicit Euler method

$$\widetilde{\mathbf{x}}^{n+2}_{(p)} = \widetilde{\mathbf{x}}^{n+1}_{(p)} + \Delta t \widetilde{\mathbf{u}}^{n+1}_{(p)}. \tag{3.33}$$

Then the material properties and body forces are evaluated

$$\rho^{n+2} = \rho(\widetilde{\mathbf{x}}_{(p)}^{n+2}); \quad \mu^{n+2} = \mu(\widetilde{\mathbf{x}}_{(p)}^{n+2}); \quad \mathbf{F}^{n+2} = \mathbf{F}(\widetilde{\mathbf{x}}_{(p)}^{n+2}). \tag{3.34}$$

and the flow equations are solved once more using the MAC method to obtain the velocity and pressure fields $\widetilde{\mathbf{u}}^{n+2}$ and $\widetilde{\mathbf{p}}^{n+2}$, respectively. Finally the quantities are updated using as simple averages as follows:

$$\begin{aligned}
\mathbf{x}_{(p)}^{n+1} &= \frac{1}{2}\left(\mathbf{x}_{(p)}^{n} + \widetilde{\mathbf{x}}_{(p)}^{n+2}\right), \\
\mathbf{u}^{n+1} &= \frac{1}{2}\left(\mathbf{u}^{n} + \widetilde{\mathbf{u}}^{n+2}\right), \\
\mu^{n+1} &= \frac{1}{2}\left(\mu^{n} + \widetilde{\mu}^{n+2}\right), \\
\rho^{n+1} &= \frac{1}{2}\left(\rho^{n} + \widetilde{\rho}^{n+2}\right).
\end{aligned} \tag{3.35}$$

It can be shown that the above procedure is equivalent to the trapezoidal rule and yields a second order accuracy in time.

Chapter 4

MODEL FOR THE MECHANICS OF LEUKOCYTE DEFORMATION

Cell deformation plays a significant role in cell adhesion (since it limits the size of the contact area, disrupts the surrounding flow field and absorbs some of the force aimed at detaching the cell), and in many other cell functions such as flow through capillaries [3]. Much study has been performed in an attempt to understand the deformation of cells and establish the constitutive mechanical relations. One of the most common techniques used is the cell-entry micro-pipette assay. As illustrated in Fig. 4.1, this assay consists of pulling a portion of the cell or the entire cell into a micro-pipette of set diameter, with a constant suction pressure. The experiments are recorded using specialized video cameras, and the distance between the leading edge of the cell and the tip of the pipette (L_p or projection length) is plotted as a function of time. From this plot and by assuming a constitutive relation for the cell mechanics, parameters for the cell mechanics of the cell can be calculated. This technique has been used in conjunction with several models to study neutrophils [3, 16, 40] and granulocytes [12] and lymphocytes [11].

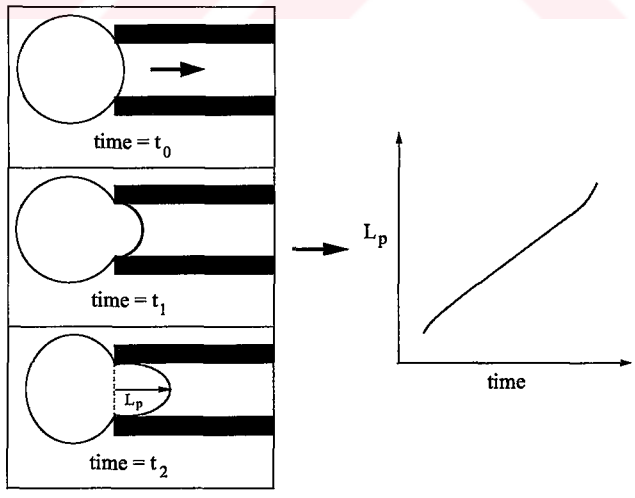

Figure 4.1: Sketch of cell-entry micro-pipette assay, and typical results.

The micro-pipette experiments are analyzed using mathematical models which are based on the observations of the mechanical behavior of the cell. If the cell flows continuously into the pipette, it behaves as a fluid. If the cell flows continuously into the pipette and stops, and the projection length is a function of suction pressure, then the cell is assumed to have some elastic behavior. If, when the forces tending to deform the cell are eliminated, the cell recovers its original shape, then the cell is either elastic or in a state of tension [37].

Theoretical efforts at constitutive modeling of the leukocytes have been punctuated by experimental studies that have periodically overturned tentatively accepted models. The evolution of the experiments and models are mentioned in Chapter 2. The nucleus has been suspected to affect the deformation of leukocytes significantly. The models of a Newtonian fluid enclosed by a membrane predict that the rate of cell entry into the pipette increases monotonically as the cell enters. However, the experiments show that the cell enters very rapidly at the beginning, then slows down, and speeds up again. In order to simulate this behavior, Tsai et al. [15] proposed a model treating the cell interior as a shear-thinning fluid, in which the viscosity of the cytoplasm decreases with increasing shear-rate. Nevertheless, other researchers have suggested that this behavior could be explained by the presence of a three layer model: the cortical shell, the cytoplasm, and a more viscous nucleus [17, 13]. This model is supported by the observation of Zhelev and Hochmuth [41] that the maximum value of the viscosity is found when about half of the nucleus is observed to be in the pipette. Udaykumar et al. [5] improved the model proposed by Dong et al. [17] and Hochmuth et al. [13] by modeling the cortical layer as an elastic membrane with a nonlinear stress-strain curve to simulate unfolding of the excess surface area of the membrane. They used a power-law shear thinning fluid for the cytoplasm. Their compound cell model approaches closely the leukocyte responses observed in some experiments. However, their shear-thinning viscosity model failed to capture the experimentally observed shear-rate response of the leukocytes.

The main idea pursued in this thesis is to view the nucleus as a significant structural entity and to investigate its effect on the dynamics of the compound cell in deformation. In this regard, one particular simplification refer to the shape of the nucleus. The nucleus can assume different forms depending on the type of leukocyte. For circulating neutrophils, which are the most abundant WBCs the nucleus is segmented, while for a lymphocyte it is

large and spherical. In this thesis, due to the simplicity of the implementation, the nucleus is modeled as a spherical structure enclosed within the cell. This situation applies more closely to lymphocytes rather than neutrophils.

The model used in this thesis has the capability of incorporating the nucleus. Furthermore, the compound cell model is improved by the addition of uniformly distributed linear springs between the nucleus and cortex in order to model the effects of the internal structures such as microtubles and microfilaments in the cytoplasm. The present model offers a large range in both complexity of the model and the number of parameters that can be used to model the overall deformation of the leukocyte without significant changes in the setup. The representation of the leukocytes as composites of fluid bodies enclosed by membranes enables the construction of alternative models by varying the number of fluid bodies, the properties of the fluids such as density and viscosity, and the material parameters for each of the membranes. This chapter illustrates the evaluation of the effects each of the elements has on the results of the simulations of micro-pipette experiments.

This chapter begins with the description of the building blocks of the model and illustrates the addition of the linear springs between the nucleus and cortex. The second subsection presents simulations of cell-entry, micro-pipette experiments, and discusses the effects that the different elements of the model have on the outcome of the simulations.

4.1 Description of the Elements in the Model

The main elements which are used to construct the mechanical models of leukocytes are Newtonian fluid bodies, pre-stressed membranes and linear springs between the nucleus and outer membrane. The model can be as simple as a Newtonian fluid enclosed by a pre-stressed membrane, or as complicated as a cytoplasm filled with an internal body connected to the outer membrane with linear springs. In order to demonstrate the capabilities of the method and at the same time keep things simple, all membranes are assumed to hold isotropic tension, and only one internal body which represents the nucleus is incorporated. Figure 4.2 demonstrates three types of models which can be constructed from these alternatives. Figure 4.2 (a) illustrates the simple cell model of the leukocyte which is comprised of a Newtonian fluid surrounded by the cortex. Figure 4.2 (b) shows the compound cell model of the leukocyte where the more viscous internal fluid body represents the nucleus.

Figure 4.2 (c) demonstrates the incorporation of the linear springs between the membrane of the internal fluid body (nucleus) and the cortex.

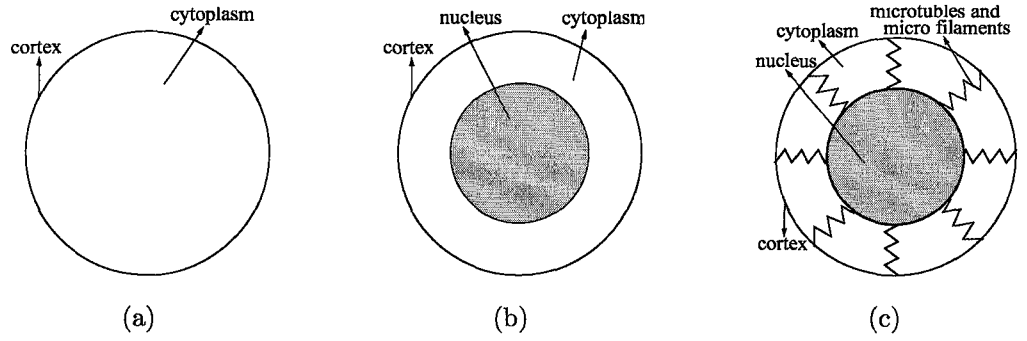

Figure 4.2: Examples of models for the mechanical properties of the leukocyte: (a) a Newtonian fluid surrounded by the cortex. ; (b) a Newtonian fluid with a more viscous Newtonian fluid inside (representing the nucleus) ; (c) Linear springs are added between outer and inner membrane to the model mentioned in (b)

The mechanics of the nuclei of leukocytes, and the interfacial tension due to the phase boundary between the membrane and surrounding fluid was explored by many researchers. Needham and Hochmuth. [40] found that the interfacial tension of the membrane of a neutrophil ranges between $0.024 - 0.038$ *dyne/cm*. Zhelev et al. [11] determined the interfacial tension of the membrane of the lymphocyte nucleus to be 0.035 *dyne/cm*. Schmidt-Schonbein et al. [4] determined that the nucleus of neutrophils is segmented and spread and occupies about 20 % of the volume of the cytoplasm. They also found that the nucleus of lymphocytes is spherical and occupies 40 % of the cytolplasm. Dong et al. [17] estimated the viscosity of the lymphocyte nucleus to be an order of magnitude larger than the viscosity of the cytoplasm.

4.1.1 Incorporation of the Linear Springs Between the Nucleus and Cortex

To improve the compound cell model (sketched in Fig. 4.2 (b)) and to better represent the response of the leukocyte to deformation, linear springs are added to the compound cell model between the membrane of the nucleus and cortex (outer membrane) as sketched in Fig. 4.2 (c). The linear springs are virtual and they connect the centroids of the front elements of the membrane of the nucleus to the corresponding centroids of the front elements

of the cortex. The computation of the force which inner springs exert on the cortex during deformation is explained in details in Appendix A.

Figure 4.3 shows the effect of the incorporated internal linear springs to the position of the co-centered nucleus. An initial perturbation in the horizontal direction is applied in order to make the nucleus off-centered with respect to the leukocyte. The fluid is initially quiscent and flow is totally driven by the internal springs. As can be seen from Fig. 4.3, the nucleus moves to the center of the leukocyte. In Fig. 4.4, the change in the error with time is demonstrated for different values of the parameter γ which is the ratio of the spring to the surface tension forces (as explained in Appendix A). The error is defined as

$$error_{co-centered} = \frac{|\Delta x_{c_{exact}} - \Delta x_{c_{comp}}|}{\Delta x_{c_{exact}}} \tag{4.1}$$

where $\Delta x_{c_{exact}}$ and $\Delta x_{c_{comp}}$ are the difference between the x-coordinates of the centroids of the nucleus (inner drop) and leukocyte (outer drop) before and after the perturbation, respectively. As can be seen in Fig. 4.4, the nucleus and cytoplasm are relaxed to their specified equilibrium state.

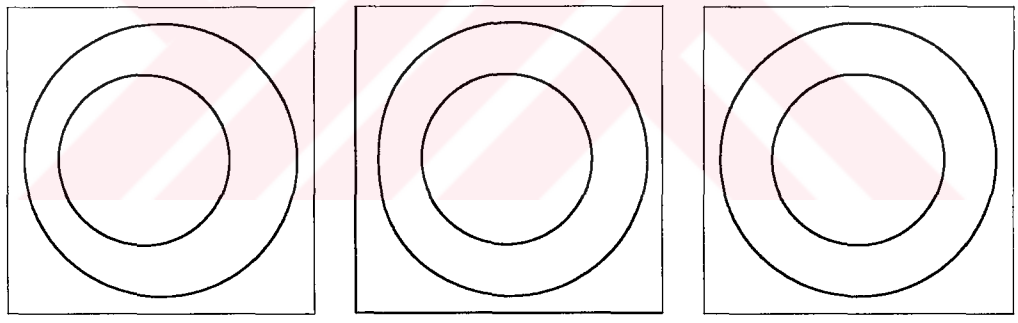

Figure 4.3: The effect of the incorporated linear springs to the position of the nucleus. Originally, the nucleus and the leukocyte are co-centered. An initial perturbation is applied to make the nucleus off-centered with respect to the leukocyte. γ is set to 10. From left to right the corresponding time frames are: 0.0 s, 0.3 s, and 1.4 s.

Figure 4.5 shows the effect of the incorporated internal linear springs to the position of the off-centered nucleus. An initial perturbation in the horizontal direction is applied in order to make the nucleus and the leukocyte co-centered. The fluid is initially quiscent and flow is totally driven by the internal springs. As can be seen from Fig. 4.5, the nucleus

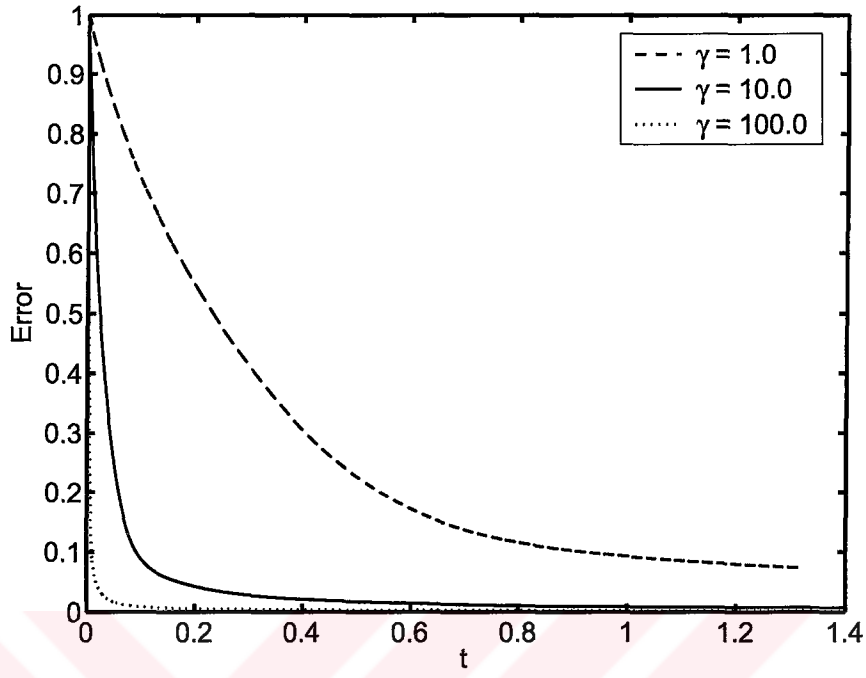

Figure 4.4: Error versus time for different value of γ.

moves to its initial position. In Fig. 4.6, the change in the error with time is demonstrated for different values of the parameter γ which is the ratio of the spring to the surface tension forces (as explained in Appendix A). The error is defined as

$$error_{off-centered} = \frac{\Delta x_{c_{comp}}}{\Delta x_{c_{exact}}} \tag{4.2}$$

where $\Delta x_{c_{exact}}$ and $\Delta x_{c_{comp}}$ are the difference between the x-coordinates of the centroids of the nucleus (inner drop) and leukocyte (outer drop) before and after the perturbation, respectively. The error, except for the case where $\gamma = 100$, tend to zero with increasing time, which proves that the model is working properly for a specified range of the parameter γ. For the case where $\gamma = 100$, there occurs instability, and the nucleus does not return to its original position.

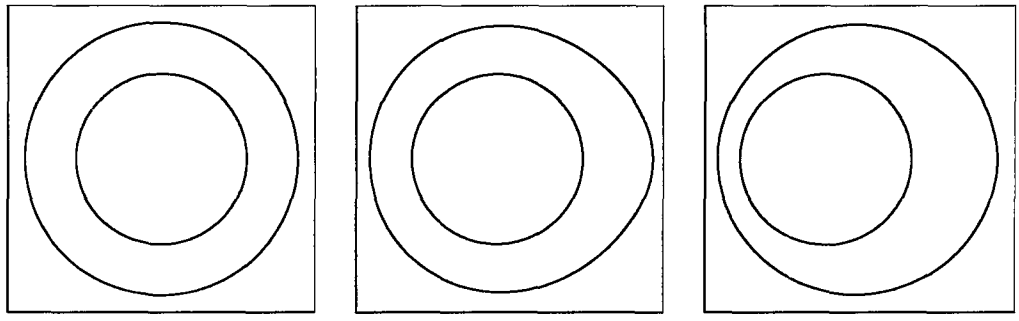

Figure 4.5: The effect of the incorporated linear springs to the position of the nucleus. Originally, the nucleus and the leukocyte are off-centered. An initial perturbation is applied to make the nucleus and the leukocyte co-centered. γ is set to 10. From left to right the corresponding time frames are: 0.0 s, 0.4 s, and 1.4 s.

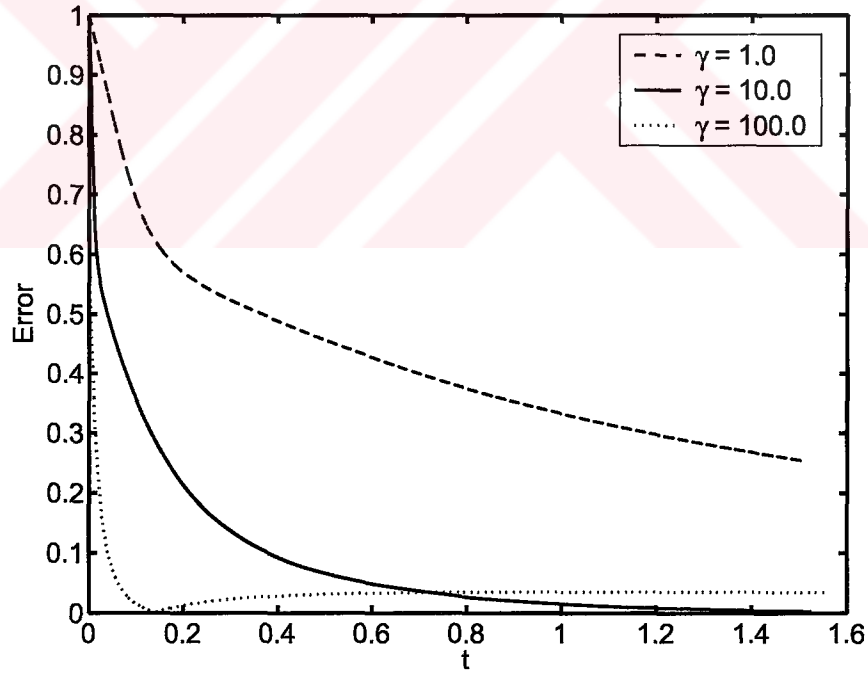

Figure 4.6: Error versus time for different values of γ.

4.2 Representative Simulations of Micro-Pipette Experiments

4.2.1 Implementation and Preliminary Considerations

The micro-pipette experiments are simulated in two dimensional domain. Fig. 4.7 shows the computational grid for the simulation of aspiration into micro-pipette. Two rectangles parallel to each other touching one end of the domain represent the walls of the micro-pipette. The fluid body representing the cell is initialized to a circle and placed near the entrance of the two rectangles.

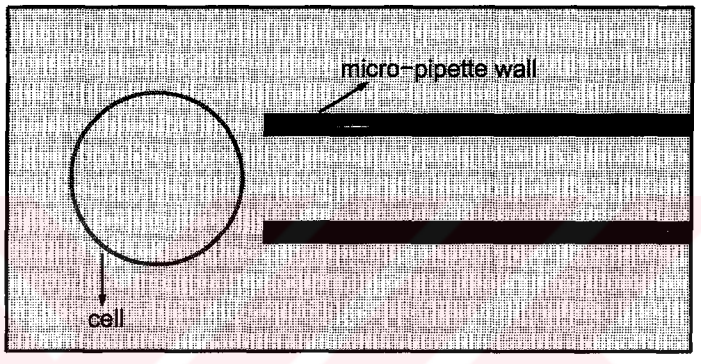

Figure 4.7: Computational grid for simulation of aspiration into micro-pipette.

The flow into the pipette is driven by a pressure difference imposed between the exit of the micro-pipette and the far-field. Thus, constant pressure boundary conditions are applied at the exit of the pipette; and on the left and right boundaries of the domain. The top and bottom boundaries are set to far-field conditions. The problem of micro-pipette aspiration is characterized by two different flow regimes. In the first regime, when the cell is not in contact with the pipette, the flow is controlled by the fluid outside the cell. A pressure gradient exists inside the pipette, and the velocity of the fluid reaches its maximum value in the gap between the walls at the tip of the pipette and the cell. When the cell makes contact with the pipette, the fluid inside the cell begins to control the flow; and the flow inside the pipette becomes plugged [37]. The experimental data is obtained once this second flow regime is established.

As mentioned in Chapter 3, the constraint on the time step Δt due to the viscous terms (Eq. 3.18) decreases with the density and the square of the uniform gird size, and the inverse

of the dynamic viscosity. The high estimates of the cytoplasmic viscosities of leukocytes (about 10^5 times that of water), and the small computational cells needed to resolve the gap between the cell and the pipette wall make this constraint more restrictive. Using the estimate of the cytoplasmic viscosity (100 Ns/m^2)mentioned above, the density of water (1000 kg/m^3) which is the same order of magnitude as the density of the cytoplasm, and 10 % of the cell diameter (assuming the diameter of a cell on the order of 10^{-6} m) for the minumum size of the computational cells, the time step must be lower than 10^{-13} s for the sloution to remain stable. Micro-pipette experiments usually occur on the order of $2 - 100$ seconds [6]; and in this case it is not possible for a simulation to be concluded in a feasible computational time.

This constraint can be avoided if the viscosity of the cytoplasm can be decreased, or if the minimum grid size or the density can be increased without significantly changing the solution. The first two parameters are very important in determining the solution. Following Agresar et al. [37], the effects of increasing the density of the fluids (the density inside the cell is assumed to be equal to the density outside the cell) on the solution was studied. Figure 4.8 shows that the solution does not depend significantly on the density. In order to make the comparison easy, in the plots of L_p vs. time, the curves are shifted to the origin so that the time is zero when the cell touches the micro-pipette. As long as the Reynolds number (Re) is small, i.e., $Re < 0.1$, the density of the fluid should not be important (in the Stokes limit, the solution is completely independent of density).

The simulations of the following section were run using a density of 10^{11} kg/m^3, since this increases the maximum allowable time step. The effective Reynolds number of these simulations is in the range $0.0001 - 0.01$. The density inside the cell is equal to the density outside the cell in the simulations.

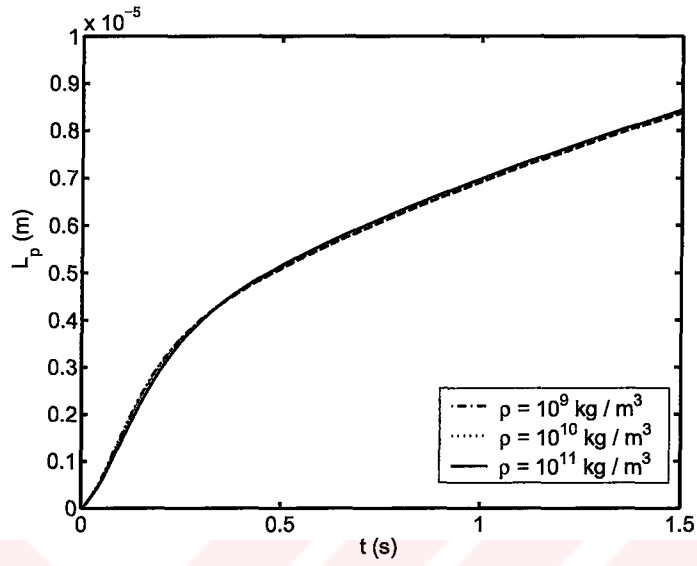

Figure 4.8: Effects of increasing density, ρ, on the curve of L_p vs. time. The viscosity inside the cell is set to 100 $kgm^{-1}s^{-1}$, the viscosity of the surrounding fluid is set to 0.1 $kgm^{-1}s^{-1}$, the radius of the cell is 4 μm, the distance between the micro-pipette walls is 2 μm, $\sigma = 2\times10^{-5}\ Nm^{-1}$, and the suction pressure is 1 kPa. The effective Reynolds numbers corresponding to the density values $10^9\ kg/m^3$, $10^{10}\ kg/m^3$, $10^{11}\ kg/m^3$ are 0.0006, 0.0082, 0.064, respectively.

4.2.2 Results and Discussion

In this section, micro-pipette aspiration experiments are simulated using various mechanical models for the leukocyte. In all the simulations, parameters on the order of those estimated for leukocytes are used. The radius of the leukocyte is set to 4 μm, and the diameter of the pipette (the distance between the bottom side of the upper rectangle and the top side of the lower rectangle) is set to 4 μm. The following section presents two cases in which the leukocyte is modeled as a Newtonian drop and is aspirated using two different suction pressures. The results of these simulations are qualitatively compared to the experimental results of Needham and Hochmuth [42]. The last section presents a comparison of the effects of the membrane pre-stressed tension, the nucleus, and the linear springs added between the nucleus and the cortex on the behavior of leukocytes during cell-entry micro-pipette

simulations.

The Leukocyte as a Newtonian Viscous Drop

The leukocyte is first modeled as a Newtonian fluid surrounded by a pre-stressed cortical shell as illustrated in Fig. 4.2 (a). The model and the simulation parameters were chosen in accordance with those used by Needham and Hochmuth [42] in order to qualitatively compare the results obtained by simulations with their experimental results. In the simulation, the surface tension σ of the membrane is set to $4 \times 10^{-5}\ N/m$; the viscosities of the surrounding and inner fluid are set to 0.1 Ns/m^2 and 100 Ns/m^2, respectively. In the computational domain, the leukocyte is located such that the distance between the leading edge of the leukocyte and the entry of the micro-pipette is 1 μm. Two suction pressures were used: 1 kPa and 2 kPa. Figure 4.9 demonstrates the snapshots in time of the pressure contours of the leukocyte entering a micro-pipette with a suction pressure of 1 kPa. The two flow regimes described in the previous section can be seen in this figure. At time $t = 0.002$ s, the flow is still controlled by the surrounding fluid (the fluid external to the leukocyte). First frame in Fig. 4.9 demonstrates a pressure gradient along the micro-pipette. At time $t = 0.04$ s, plugged flow is observed. Second frame in Fig. 4.9 shows that there is a pressure gradient propagating towards the interior of the leukocyte. Furthermore, the maximum pressure is located at the tip of the micro-pipette where the leukocyte makes contact. In the last two frames, the pressure gradient is still visible in the projection of the leukocyte inside the micro-pipette.

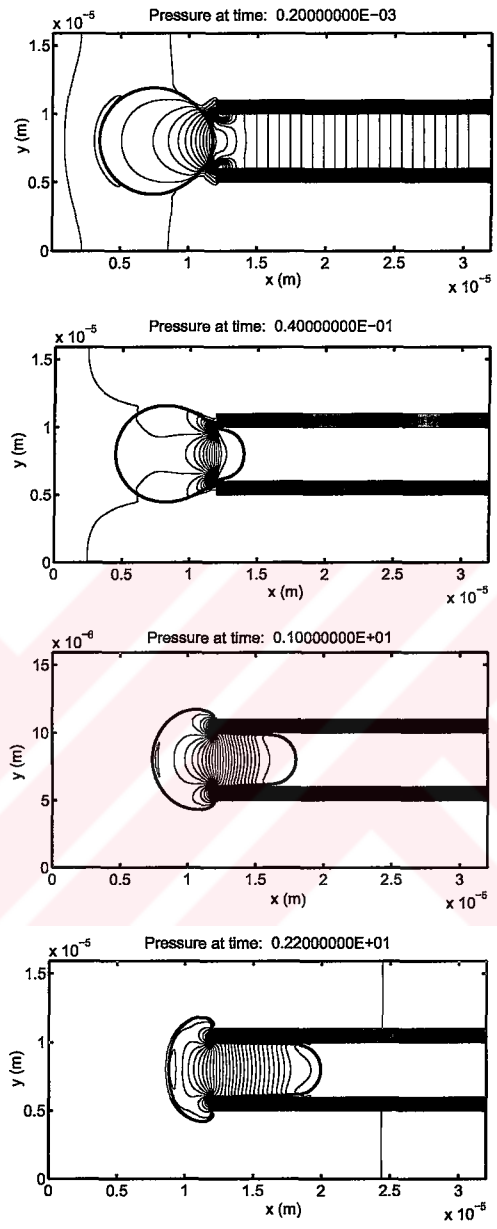

Figure 4.9: Pressure contours during entrance of the leukocyte modeled as a Newtonian fluid into the micro-pipette with a suction pressure of 1 kPa. From top to bottom the corresponding time frames are: 0.003 s, 0.03 s, 1.0 s, and 2.2 s. The mechanical parameters of the leukocyte are $\sigma = 4 \times 10^{-5}\ N/m$ and $\mu_{cytoplasm} = 100\ Nsm^{-2}$.

The changes in the shape of the leukocyte (modeled as a Newtonian drop) during the aspiration process as seen in Fig. 4.9 can be compared qualitatively with the experimental results presented by Needham and Hochmuth [42] and Tsai et al. [15]. Although the experimental results were presented for the suction pressure about 0.5 kPa, some similarities still exist between the computed shapes shown in Fig. 4.9 and the experimental results. As seen in Fig. 4.9 the leading edge of the leukocyte is rounded. The outer part of the leukocyte remains relatively spherical (circular in two dimensional simulation) during the initial entry, and flattens into a bean-like shape after some time. The angle between the tip of the micro-pipette and the outer portion of the leukocyte, however, differs between the simulations and the experiments. In the results of the simulations the curved outer part of the leukocyte ends more abruptly at the top of the tip of the micro-pipette, at which place it becomes flat (following the shape of the micro-pipette.) On the other hand, Needham and Hochmuth [42] and Tsai et al. [15] have shown that the curved portion of the leukocyte ends in the center of the tip of the micro-pipette with a larger contact angle. This difference is not surprising since the model of a Newtonian drop has been demonstrated to capture only some of the behavior of leukocytes entering into a micro-pipette [42, 11]. The contact angle between the leukocyte and the tip of the micro-pipette probably depends on the magnitude of the suction pressure with the larger suction pressure causing a more aggressive change in the shape. A fact which could have an effect on this contact angle is that the tips of the micro-pipettes used in the experiments are rounded, whereas in the simulations they are assumed to be squared. In order to capture the behavior of the shape of the leukocyte observed experimentally, linear springs between the cortex and the nucleus membrane are incorporated into the compound cell model (corresponding simulations will be mentioned later in this chapter).

Figure 4.10 shows the projection length of the leukocyte modeled as a Newtonian fluid plotted as a function of time. As it can be seen from this figure, the higher suction pressure increases the rate of entry at intermediate times to about twice the rate at the lower suction pressure. This trend agrees with those of the experimental results of Needham and Hochmuth [42]. However, the absolute rates of entry observed in the simulations are slower than the ones observed by the experimentalists. For a suction pressure of 1 kPa, the experimental results of Needham and Hochmuth [42] show that the cell completely entered the

micro-pipette by 2 s, whereas in the present simulations there is still a part of the leukocyte outside the micro-pipette at time equal to 2.2 s as seen in Fig. 4.9(d). The most likely reason for this slower rate of entry is that the present simulations are two dimensional. Thus, only qualitative comparisons between the present simulations and experimental results are meaningful. Another reason for this slower rate of entry concerns with the finite resolution of the small gap between the cell and micro-pipette wall. The computational cell representing the small gap effectively reduces the distance between the micro-pipette walls (the radius of the micro-pipette in 3-d). The data of Zhelev and Hochmuth [11] show that a 0.3 μm decrease in micro-pipette radius at approximately the same suction pressures reduced the rate of entry of the cell significantly. In the simulation presented here, the length of the computational cell between the cell surface and the micro-pipette is 0.125 μm. However, a case in which the length of a computational cell was set to 0.0625 was also tested (so the effective distance between the micro-pipette walls are larger than in the previous case), and the rate of entry decreased slightly. Therefore, the effective distance between the micro-pipette walls is not likely to be the cause of the slower rate of entry.

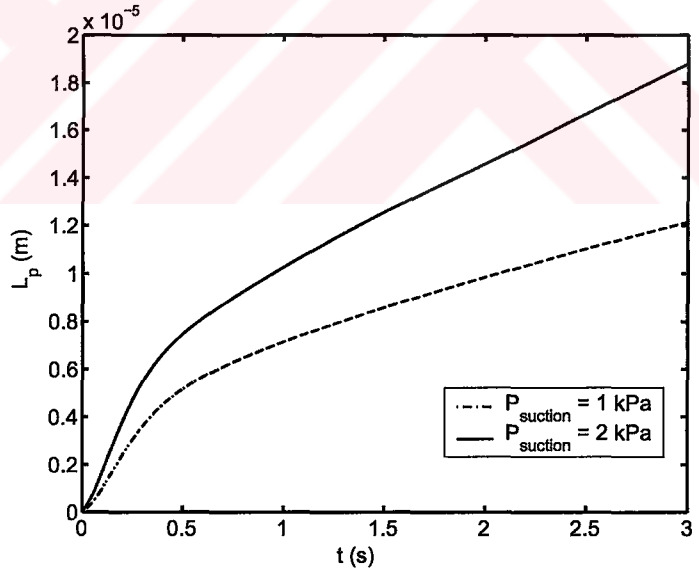

Figure 4.10: Projection length vs. time for a leukocyte models as a Newtonian drop aspirated at two different suction pressures. Mechanical parameters are the same as in Fig. 4.9.

Another explanation for the slower rate of entry of the leukocyte into micro-pipette

obtained in the simulations concerns with the boundary conditions applied on the micro-pipette walls. In the simulations, no-slip boundary conditions were imposed at the micro-pipette walls, whereas the experimentalists assumed full-slip boundary conditions in the interpretation of their data. The lubrication layer that likely exists between the cell and micro-pipette walls enables the cell to slide during entry into micro-pipette which could possibly be the reason that the rate of entry obtained from experimental data is larger than the one obtained in the simulations. Further studies are required to determine the proper treatment of the interaction of the cell surface with the micro-pipette wall.

Effects of Different Models for the Mechanics of Leukocytes on Micro-pipette Aspiration Experiments

In this section three different models of the leukocyte as sketched in Fig. 4.2 are compared to each other. These models are namely a Newtonian fluid encapsulated by a pre-stressed membrane (Model 1), a Newtonian fluid including a more viscous nucleus inside (Model 2), and a Newtonian fluid with a more viscous nucleus which includes liner springs between the outer and inner membranes (Model 3). The mechanical parameters used in the simulations for the three models are shown in Table 4.1. The parameters in the second model are on the order of those measured for lymphocytes [11]. In the last model, the parameter γ (the ratio of the inner spring to the surface tension forces) is chosen based on the cell squeezing analysis presented in the Appendix A. All simulations in this section are run at suction pressures of 2 kPa.

Figure 4.11 shows the evolution of the shapes of the leukocytes simulated with three different models. As seen in Fig. 4.11, the different mechanical models affect both the shape of the cells and the contact angle between the tip of the pipette and the outer portion of the cell. Model 3, which includes the uniformly distributed linear springs between the cortex and the nucleus, compares to experimental data better in a way that the contact angle between the tip of the pipette and the outer portion of the cell is larger than the other two models.

In the later time steps of the simulations, some problems are observed because the mechanical parameters which were evaluated from three dimensional experiments are used in two dimensional simulations. For Model 1 and Model 2, the problem is that the surface

Mechanical parameters	**Model 1**	**Model 2**	**Model 3**
Surface tension (outer membrane) (N/m)	10^{-4}	4×10^{-5}	4×10^{-5}
Surface tension (inner membrane) (N/m)	-	10^{-4}	10^{-4}
Viscosity (surrounding fluid) (Ns/m^2)	0.1	0.1	0.1
Viscosity (cytoplasma) (Ns/m^2)	100	10	10
Viscosity (nucleus) (Ns/m^2)	-	100	100
Density (all fluids) (kg/m^3)	10^{11}	10^{11}	10^{11}
(inner spring forces)/(surface tension forces)	-	-	1

Table 4.1: The mechanical parameters of the three different models representing the leukocyte used in the simulation.

tension forces of the membranes are not big enough to prevent the outer part of the leukocyte (which is not enetered into the micro-pipette yet) from bending. This situation can be seen in Figure 4.12. In Model 3, the inner spring forces causes instability during the excess deformation of the leukocyte. These problems will probably dissapear when the simulations are going to be performed in three dimensional domains.

Figure 4.13 shows the projection lengths of the cells as a function of time for the three models representing the leukocyte. Figure 4.13 illustrates that the cell with a less viscous cytoplasm and a more viscous nucleus (Model 2 and Model 3) enters the micro-pipette more rapidly than the cell modeled as a Newtonian fluid enclosed by a pre-stress cortex (Model 1). This higher rate of entry of the compound cell model (Model 2 and Model 3) is also observed in micro-pipette experiments with leukocytes [42], but the characteristics of the projection length vs time curves obtained from the micro-pipette experiments is similar to that of Model 1. In case of Model 2 and Model 3, the characteristics of the projection length vs. time curve of Model 1 is not observed. This situation probably occurs because the simulations are performed in two dimensional computational domain.

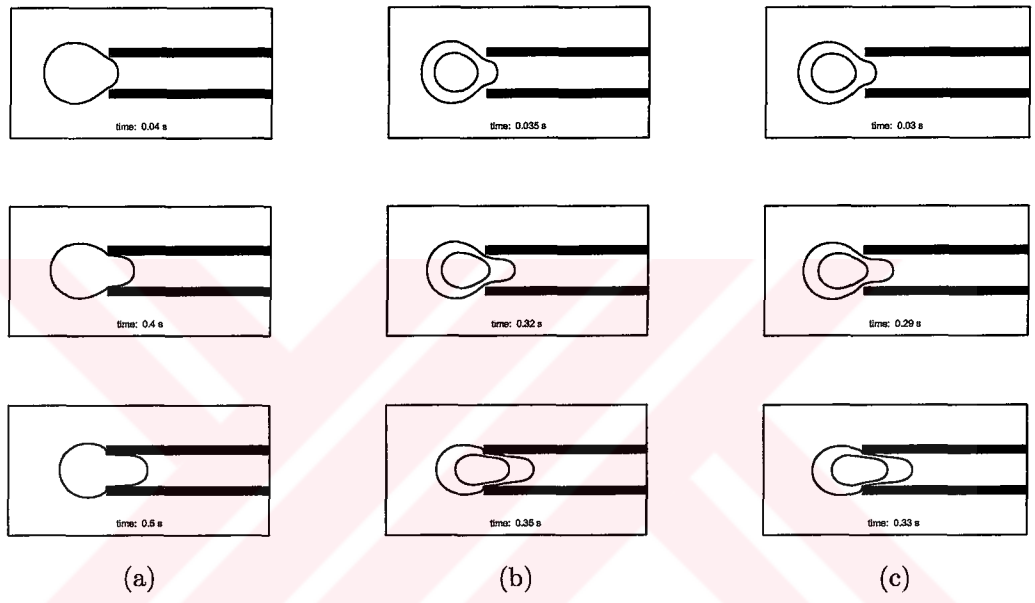

Figure 4.11: Evolution of the shape of the leukocyte entering a micro-pipette with a suction pressure of 2 kPa using three different mechanical models: a) Model 1: A Newtonian fluid enclosed by a pre-stressed cortex ; b) Model 2: A Newtonian fluid with a more viscous Newtonian fluid inside (representing the nucleus) ; c) Model 3: Linear springs are added between outer and inner membrane to the Model 2.

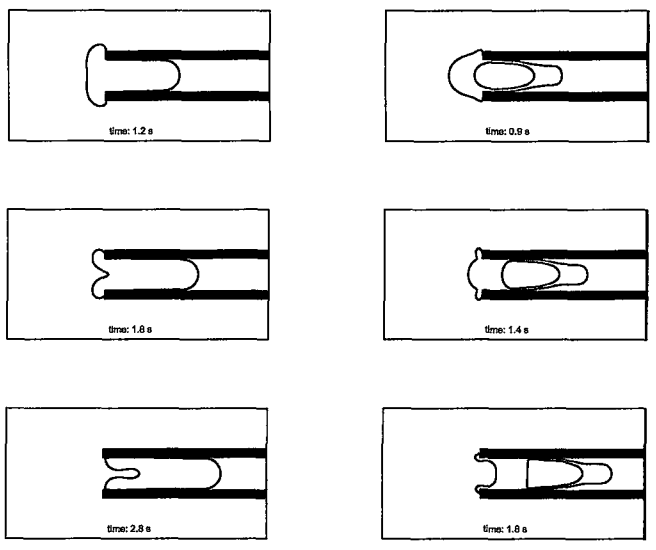

Figure 4.12: Evolution of the shape of the leukocyte during aspiration into a micro-pipette with a suction pressure of 2 kPa. The mechanical models representing the leukocyte are: a) Model 1: A Newtonian fluid enclosed by a pre-stressed cortex ; b) Model 2: A Newtonian fluid with a more viscous Newtonian fluid inside (representing the nucleus)

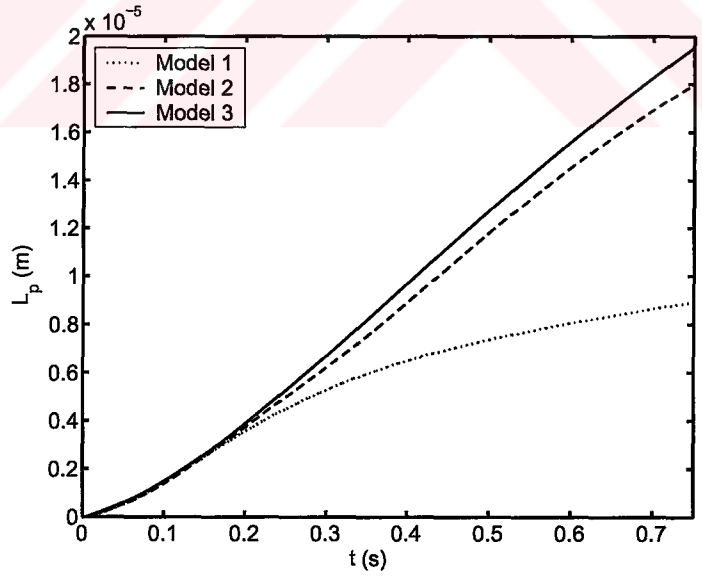

Figure 4.13: Projection length of the leukocyte into micro-pipette as a function of time for the three different models.

Chapter 5

CELL ADHESION

Leukocyte adhesion under flow in the small vessels is mediated by binding between the cell surface receptors and complementary ligands expressed on the surface of the endothelium. Adhesion of leukocytes to endothelium starts by migration of the leukocyte from the blood stream toward the vessel surface. This may be followed by primary adhesion, rolling or permanent adhesion. The significance of these processes are mentioned in Chapter 1. In this thesis, a multi-scale model is developed in order to study the adhesion of leukocytes on a substrate. The leukocyte model which includes the nucleus and the linear springs between the nucleus and cortex is used in the simulations of this chapter.

This chapter begins with the overview of the multi-scale model. Section 5.2 and 5.3 describe the macro- and micro-scale models, respectively. Section 5.4 and 5.5 present an analysis and the integration procedure of the kinetic equation which is described in Section 5.3. Section 5.6 describes the coupling of the macro- and micro-models. Finally, the last section presents simulations of cell detachment and rolling cases and discusses the effects of the inner springs between the cortex and nucleus on the outcome of the simulations.

5.1 Model Overview

A multi-scale model which accounts for both macroscopic (continuum) and microscopic (receptor-ligand) levels of the adhesion process is necessary in order to build a comprehensive modeling framework. Recently, N'Dri et al. [43] have implemented such an approach, but their leukocyte model needs to be improved. In this thesis, a multi-scale model similar to that of the N'Dri et al. [43] is used and the leukocyte model is improved by the addition of the linear springs between the nucleus and cortex. The multi-scale model is composed of two parts, namely, the micro-model and the macro-model. The macroscopic part deals with the deformation of the leukocyte and the microscopic part accounts for the adhesion process. A sketch of the adhesion model is illustrated in Fig. 5.1. It should be noted that

the receptors on the cell surface and the ligands on the substrate surface are plotted bigger than their normal scaled sizes in order to better represent the phenomena.

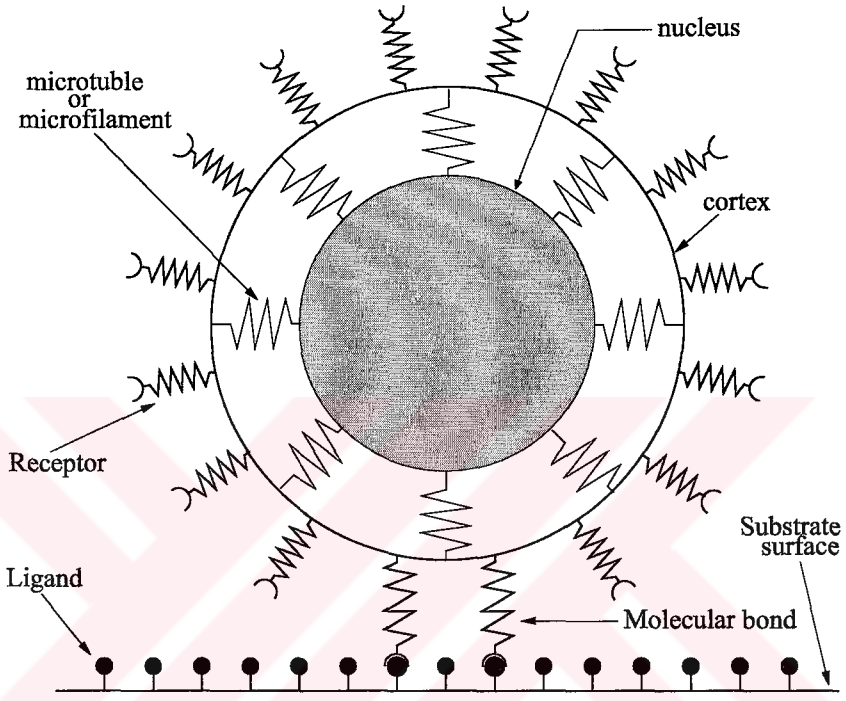

Figure 5.1: Sketch of the adhesion model.

5.2 Macro-Scale Model

The macro-scale model deals with the deformation of the leukocyte where the macroscopic problem is composed of a shear flow over a leukocyte which is located close to a flat surface of a two dimensional tube. The solution of the macroscopic problem yields information about the location of the cell membrane, and velocity and pressure in the entire computational domain. The information about the location of the cell membrane obtained from the macro-model is transmitted to the micro-model.

The bond force is incorporated into the macro-model by adding it to the surface tension.

So, the Eq.(3.24) becomes

$$\mathbf{f}_{(l)} = \left(\sigma_s \kappa_{(l)} + F_{b(l)}\right) \mathbf{n}_{(l)} \Delta s_{(l)} \tag{5.1}$$

where $F_{b(l)}$ is the total bond force of the interface element (l) and the other parameters are as described in Chapter 3.

5.3 Micro-Scale Model

The interaction between the cell and substrate surface at the receptor-ligand level is analyzed with the model proposed by Dembo et al. [2]. In this model, a molecular bond is treated as a spring, and the force of a bond f_b is given by

$$f_b = -\sigma_s(y_m - \lambda), \tag{5.2}$$

$$F_b = N_b f_b, \tag{5.3}$$

where σ_s is the spring constant, y_m and λ are the actual and equilibrium lengths of a bond, F_b is the total bond force, and N_b is the bond density. The kinetic equation which describes the formation and dissociation of bonds is given by the following first order differential equation:

$$\frac{dN_b}{dt} = k_f(N_l - N_b)(N_r - N_b) - k_r N_b, \tag{5.4}$$

where N_b is the bond density, k_r and k_f are the reverse and forward reaction rate coefficients, respectively. N_l is the initial ligand density on the surface, and N_r is the initial density of receptors on the cell membrane. The expressions which relate the forward reaction rate k_f and the reverse reaction rate k_r to the vertical separation distance y_m between the receptor's position on the cell surface and the surface of the substrate are given by Dembo et al. [2] as

$$k_r = k_{ro} \exp \frac{(\sigma_s - \sigma_{ts})(y_m - \lambda)^2}{2k_b T}, \tag{5.5}$$

$$k_f = k_{fo} \exp \frac{-\sigma_{ts}(y_m - \lambda)^2}{2k_b T}, \tag{5.6}$$

where $k_b T$ is the thermal energy (product of the Boltzmann constant and temperature), σ_s is the spring constant and σ_{ts} is the transition state spring constant. The subscript

o denotes the rates of reactions that occur at the springs equilibrium length. The initial condition to Eq.(5.4) is obtained by solving the following equation:

$$k_{fo}(N_l - N_{bo})(N_r - N_{bo}) - k_{ro}N_{bo} = 0, \tag{5.7}$$

where N_{bo} is the initial bond density, k_{fo} and k_{ro} are the equilibrium forward and reverse reaction rates, respectively. The bond density N_b is computed from the kinetic equation (Eq.(5.4)) using a 4^{th} order Runge-Kutta method and an analytical solution which will be described later in this chapter.

5.4 Analysis of the Kinetic Equation

This section presents a detailed analysis of the kinetic equation (Eq.(5.4)). The variation of the bond density N_b with time and actual bond length for different values of the micro-model parameters are demonstrated. Table 5.1 shows the estimates for the micro-model parameters.

Parameter	Value range	Typical value	References
N_r (m^{-2})	$(2.0 - 5.0) \times 10^{14}$	5.0×10^{14}	[26]
N_l (m^{-2})	$(2.0 - 5.0) \times 10^{14}$	5.0×10^{14}	[44]
k_{fo} $(m^2 s^{-1})$	$10^{8} - 10^{-18}$	10^{-18}	[29]
k_{ro} (s^{-1})	$10^{-11} - 10$	0.1	[8]
σ_s (N/m)	$(0.005 - 10) \times 10^{-3}$	5×10^{-3}	[2]
σ_{ts} (N/m)	$(0.0048 - 9.5) \times 10^{-3}$	4.5×10^{-3}	[2]
λ (m)	$(1 - 50) \times 10^{-8}$	5×10^{-8}	[26]
k_bT $(Joule)$	$(3.8 - 4.1) \times 10^{-21}$	3.8×10^{-21}	[8]

Table 5.1: Estimates for the micro-model parameters

The definitions and appropriate scaling operations for the dimensionless micro-model parameters which are used in the analysis are shown in Table 5.2. These quantities are made non-dimensional by using the reference time scale (τ_r), the reference length scale (λ_r) and the reference bond density (N_{br}). The reference time and length scales are taken as

the inverse of the typical value of the equilibrium reverse reaction rate $\tau_r = 1/k_{ro} = 10\ s$ and the typical value of the equilibrium bond length $\lambda_r = 5 \times 10^{-8}\ m$, respectively. The reference bond density is taken as the equilibrium bond density corresponding to the typical parameters given in Table 5.1 and is computed as $N_{br} = 2.48 \times 10^{12}\ m^{-2}$.

Symbol	**Definition**	**Scaling**
t^*	Dimensionless time	$t^* = t\tau_r$
N_b^*	Dimensionless bond density	$N_b^* = N_b/N_{br}$
y_m^*	Dimensionless distance from surface	$y_m^* = y_m/\lambda_r$

Table 5.2: Dimensionless micro-model parameters used in the analysis

5.4.1 Variation of the Bond Density N_b with Ligand Density N_l and Receptor Density N_r

In this case, the values of all parameters other than the receptor density N_r are set to their typical values given in Table 5.1. The variation of the bond density with time and the vertical distance from surface are demonstrated in Fig. 5.2 and Fig. 5.3, respectively.

Figure 5.2 shows that for a specified time an increase in the receptor density N_r increases the bond density N_b. Figure 5.3 demonstrates that the bond density N_b reaches a maximum when the vertical distance of the membrane from the substrate surface (y_m) is equal to the equilibrium bond length λ.

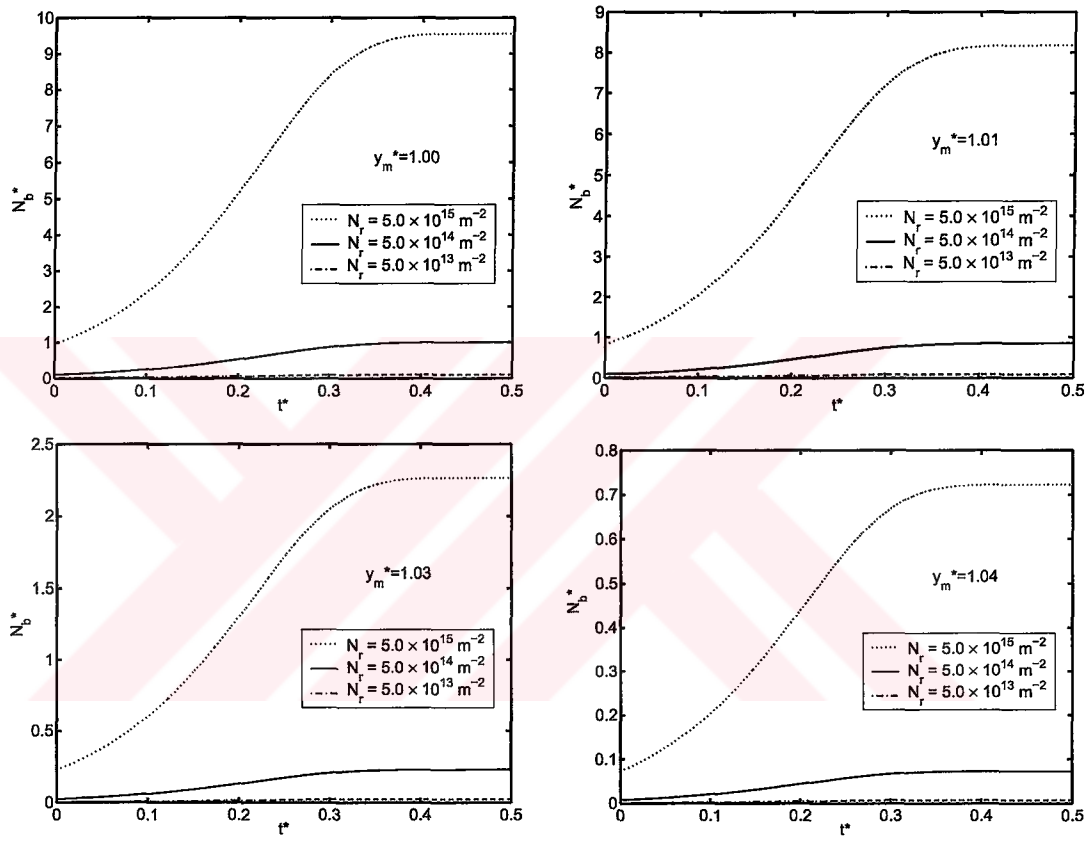

Figure 5.2: Effect of the receptor density N_r on the bond density N_b. The variation of the bond density with time is examined at four different locations (from surface).

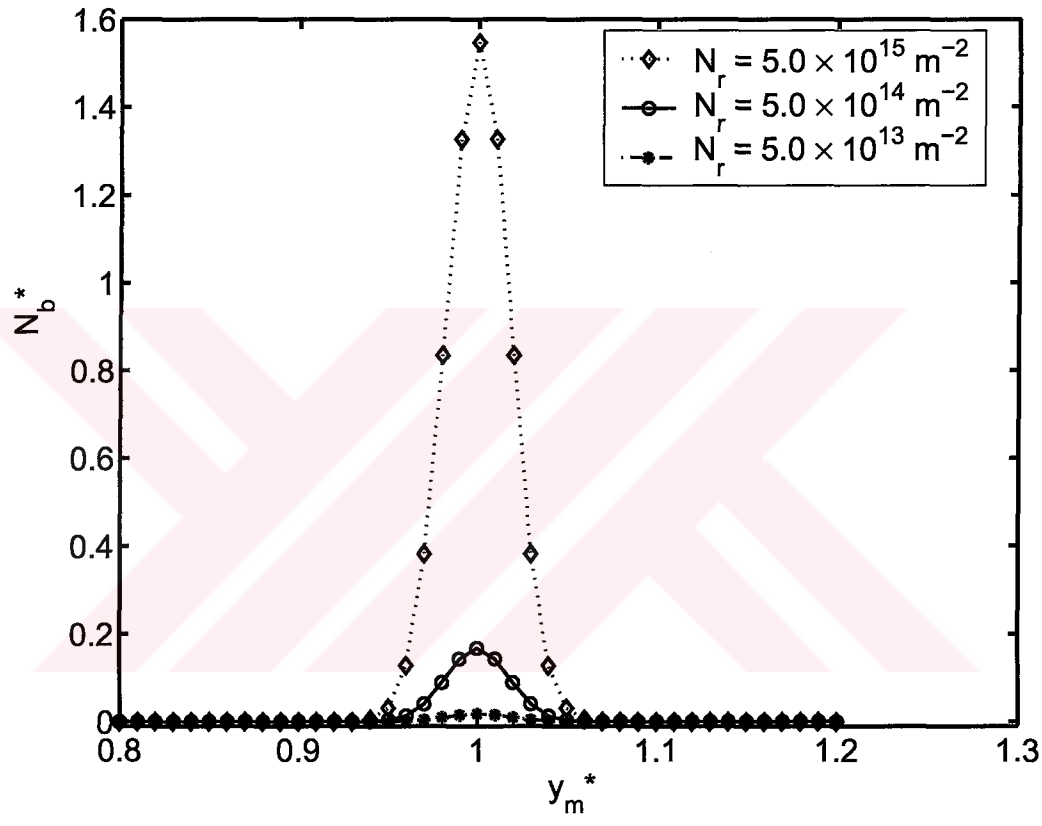

Figure 5.3: Effect of the receptor density N_r on the bond density N_b. The variation of the bond density with the distance from surface is demonstrated.

5.4.2 Variation of the Bond Density N_b with the Equilibrium Reverse Reaction Rate k_{ro}

In this case, the values of all all parameters other than the equilibrium reverse reaction rate k_{ro} are set to their typical values given in Table 5.1. The variation of the bond density with time and the vertical distance from surface are demonstrated in Fig. 5.4 and Fig. 5.5.

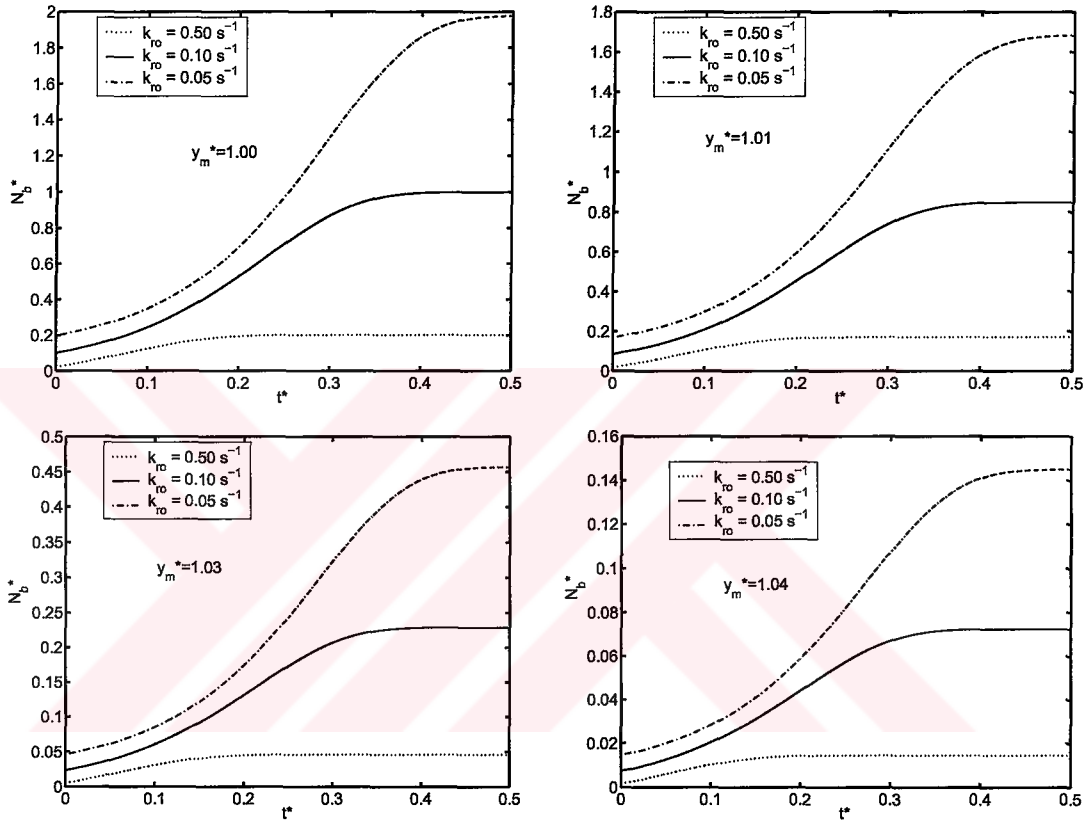

Figure 5.4: Effect of the equilibrium reverse reaction rate k_{ro} on the bond density N_b. The variation of the bond density with time is examined at four different locations (from surface).

Figure 5.4 shows that for a specified time an increase in the equilibrium reverse reaction rate k_{ro} decreases the bond density N_b. Figure 5.5 demonstrates that the bond density N_b reaches a maximum when the vertical distance of the membrane from the substrate surface (y_m) is equal to the equilibrium bond length λ.

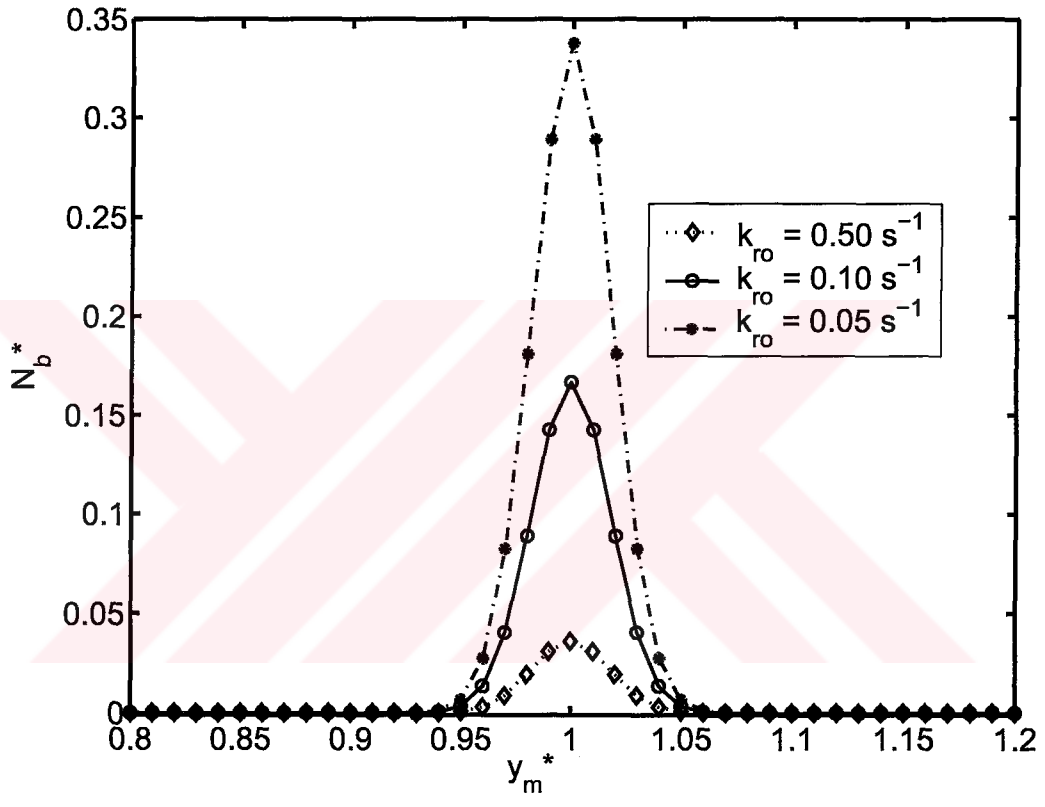

Figure 5.5: Effect of the equilibrium reverse reaction rate k_{ro} on the bond density N_b. The variation of the bond density with the distance from surface is demonstrated.

5.4.3 Variation of the Bond Density N_b with the Equilibrium Forward Reaction Rate k_{fo}

In this case, the values of all all parameters other than the equilibrium forward reaction rate k_{fo} are set to their typical values given in Table 5.1. The variation of the bond density with time and the vertical distance from surface are demonstrated in Fig. 5.6 and Fig. 5.7

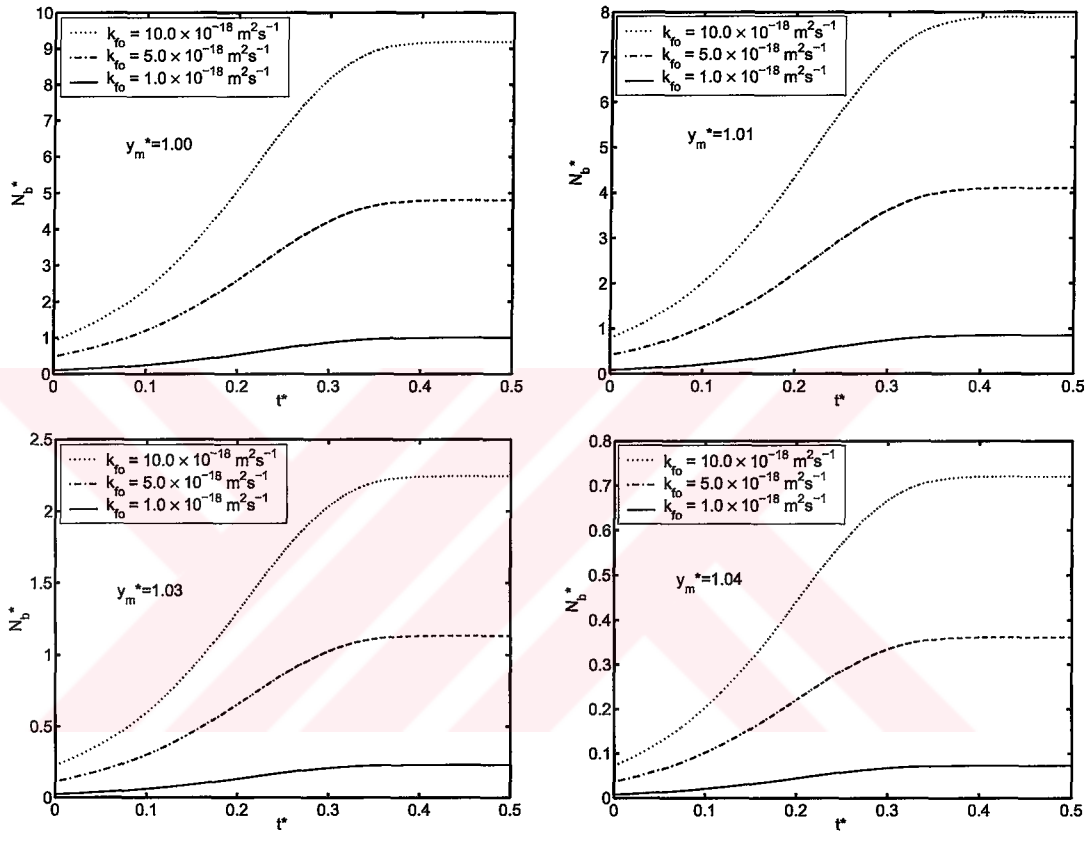

Figure 5.6: Effect of the equilibrium forward reaction rate k_{ro} on the bond density N_b. The variation of the bond density with time is examined at four different locations (from surface).

Figure 5.6 shows that for a specified time an increase in the equilibrium forward reaction rate k_{fo} increases the bond density N_b. Figure 5.7 demonstrates that the bond density N_b reaches a maximum when the vertical distance of the membrane from the substrate surface (y_m) is equal to the equilibrium bond length λ.

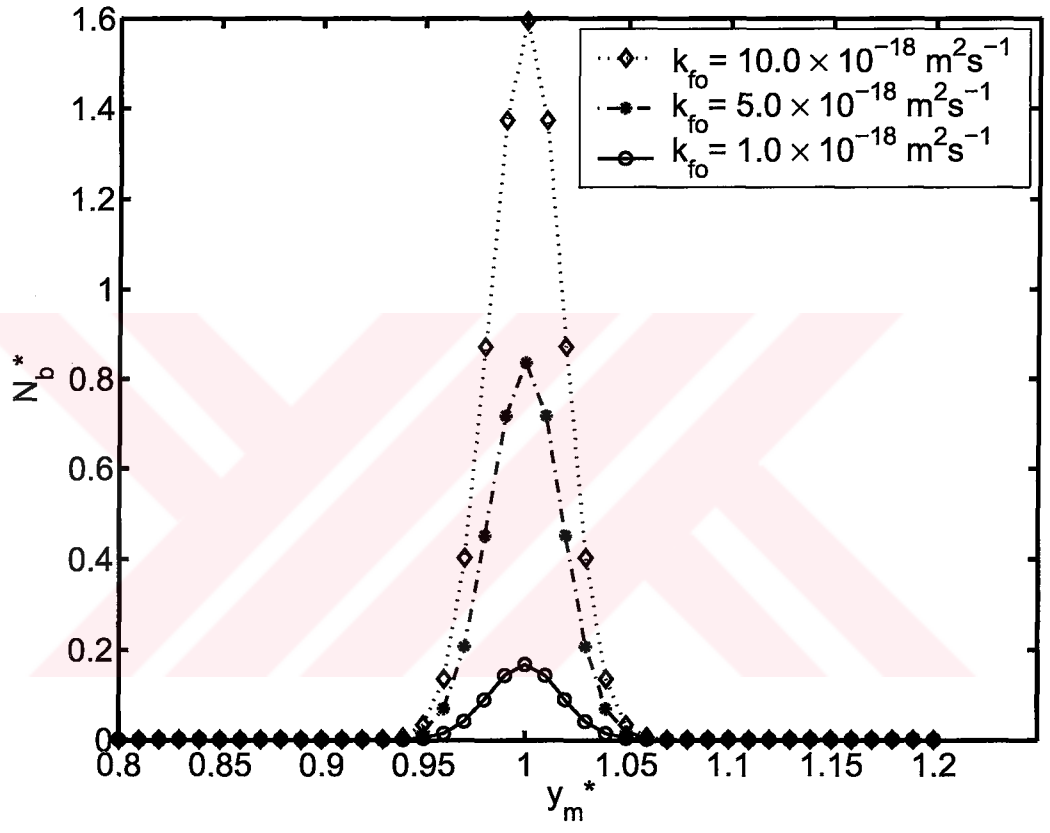

Figure 5.7: Effect of the equilibrium forward reaction rate k_{ro} on the bond density N_b. The variation of the bond density with the distance from surface is demonstrated.

5.4.4 Variation of the Bond Density N_b with the Spring Constant σ_s

In this case, the values of all all parameters other than the spring constant σ_s are set to their simulation values given in Table 5.1. The variation of the bond density with time and the vertical distance from surface are demonstrated in Fig. 5.8 and Fig. 5.9

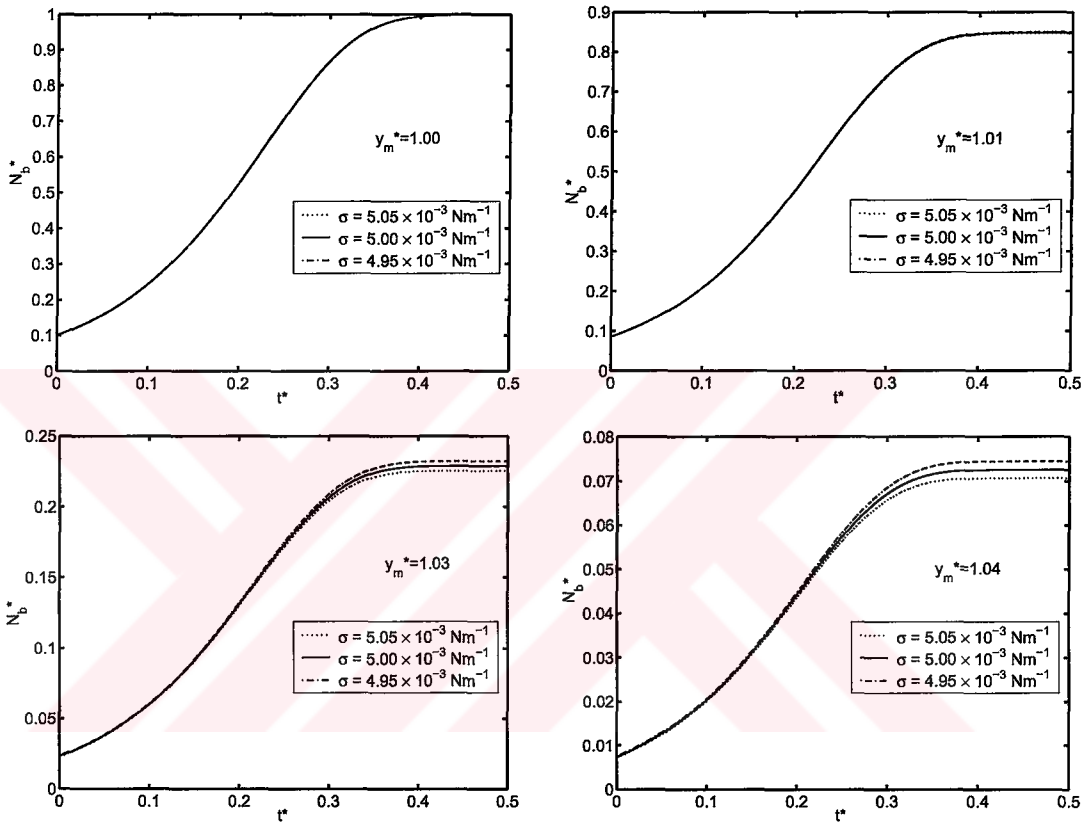

Figure 5.8: Effect of the spring constant σ_s on the bond density N_b. The variation of the bond density with time is examined at four different locations (from surface).

Figure 5.8 (figures on the bottom) shows that for a specified time an increase in the spring constant σ_s decreases the bond density N_b. Figure 5.9 demonstrates that the bond density N_b reaches a maximum when the vertical distance of the membrane from the substrate surface (y_m) is equal to the equilibrium bond length λ.

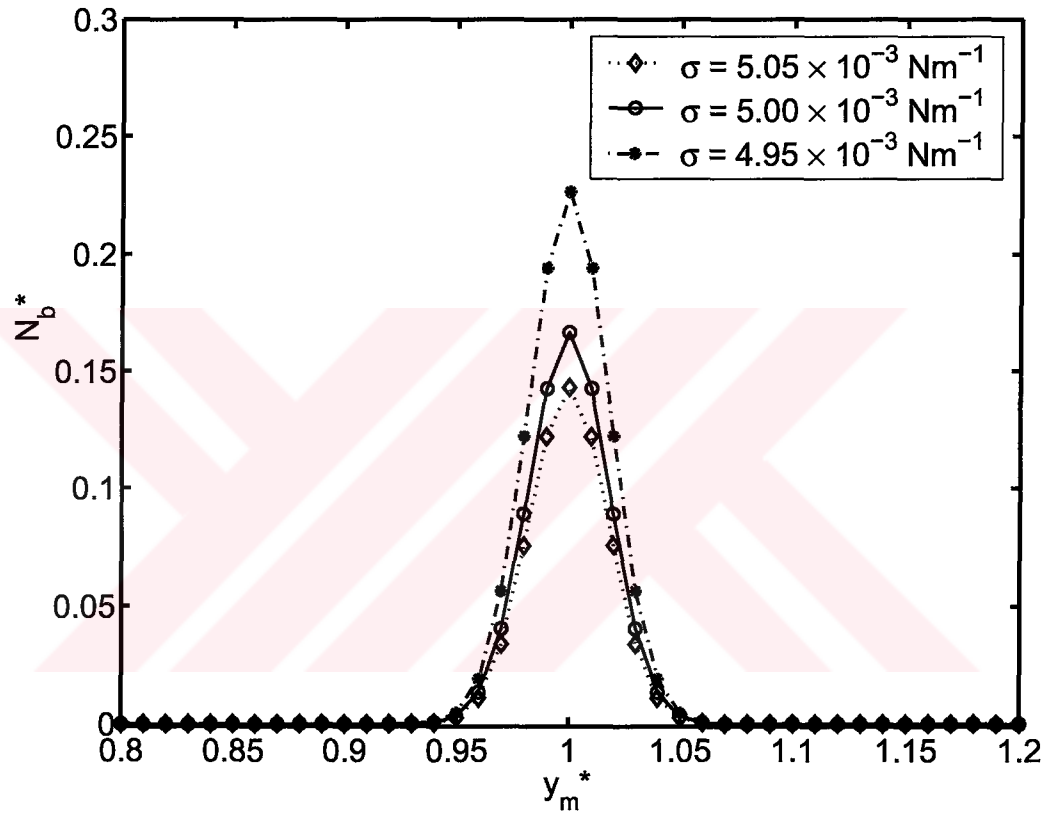

Figure 5.9: Effect of the spring constant σ_s on the bond density N_b. The variation of the bond density with the distance from surface is demonstrated.

5.4.5 Variation of the Bond Density N_b with the Transition State Spring Constant σ_{ts}

In this case, the values of all all parameters other than the transition state spring constant σ_{ts} are set to their typical values given in Table 5.1. The variation of the bond density with time and the vertical distance from surface are demonstrated in Fig. 5.10 and Fig. 5.11

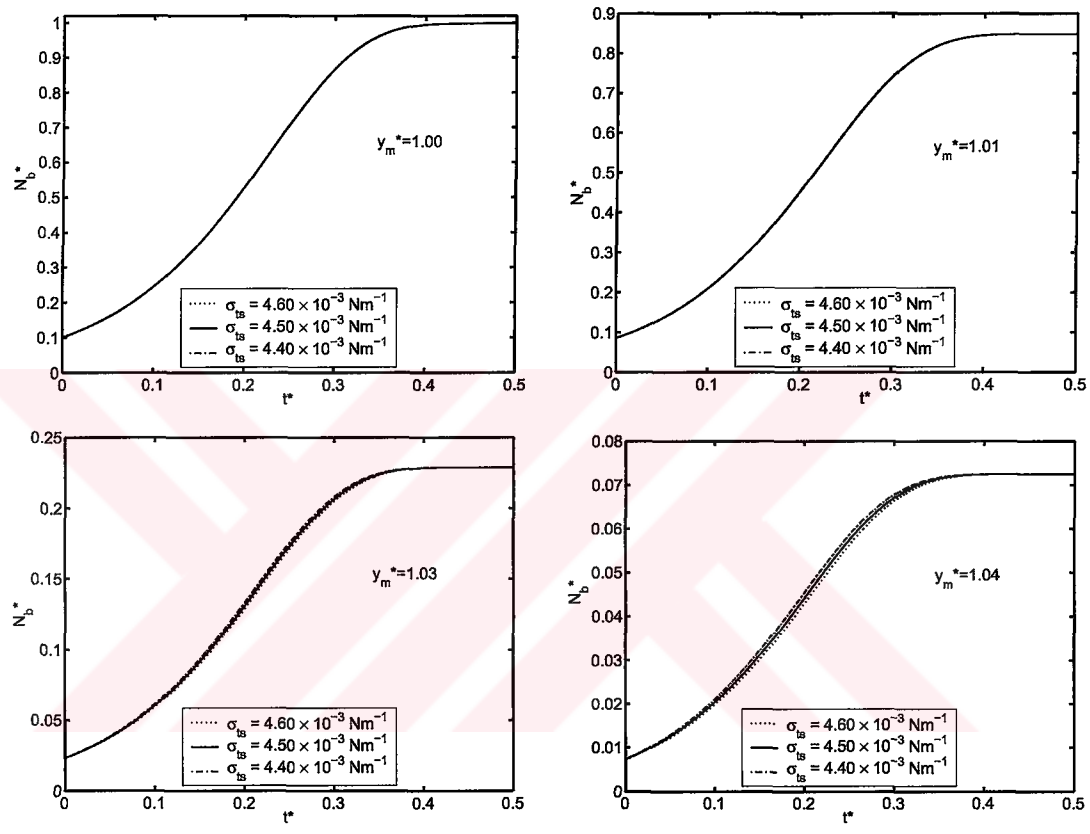

Figure 5.10: Effect of the transition state spring constant σ_{ts} on the bond density N_b. The variation of the bond density with time is examined at four different locations (from surface).

Figure 5.10 (figures on the bottom) shows that for a specified time an increase in the transition state spring constant σ_{ts} increases the bond density N_b. Figure 5.11 demonstrates that the bond density N_b reaches a maximum when the vertical distance of the membrane from the substrate surface (y_m) is equal to the equilibrium bond length λ.

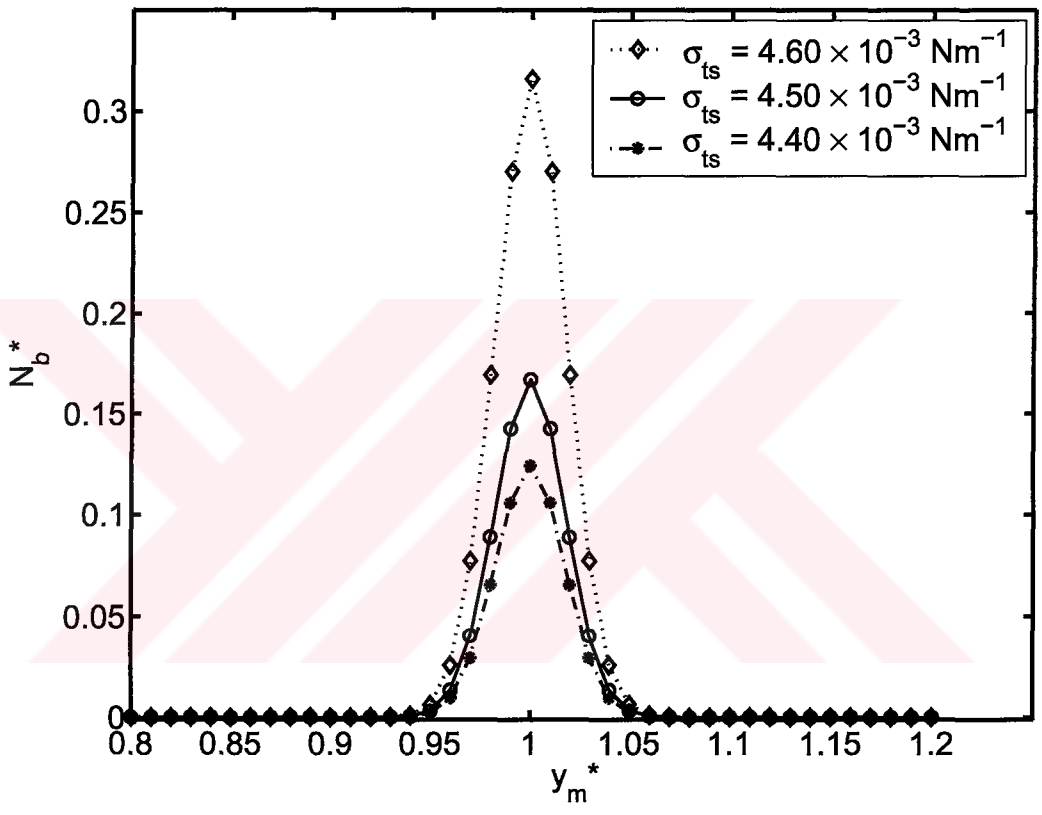

Figure 5.11: Effect of the transition state spring constant σ_{ts} on the bond density N_b. The variation of the bond density with the distance from surface is demonstrated.

5.4.6 Variation of the Bond Density N_b with the Equilibrium Bond Length λ

In this case, the values of all all parameters other than the equilibrium bond length λ are set to their typical values given in Table 5.1. The variation of the bond density with time and the vertical distance from surface are demonstrated in Fig. 5.12 and Fig. 5.13

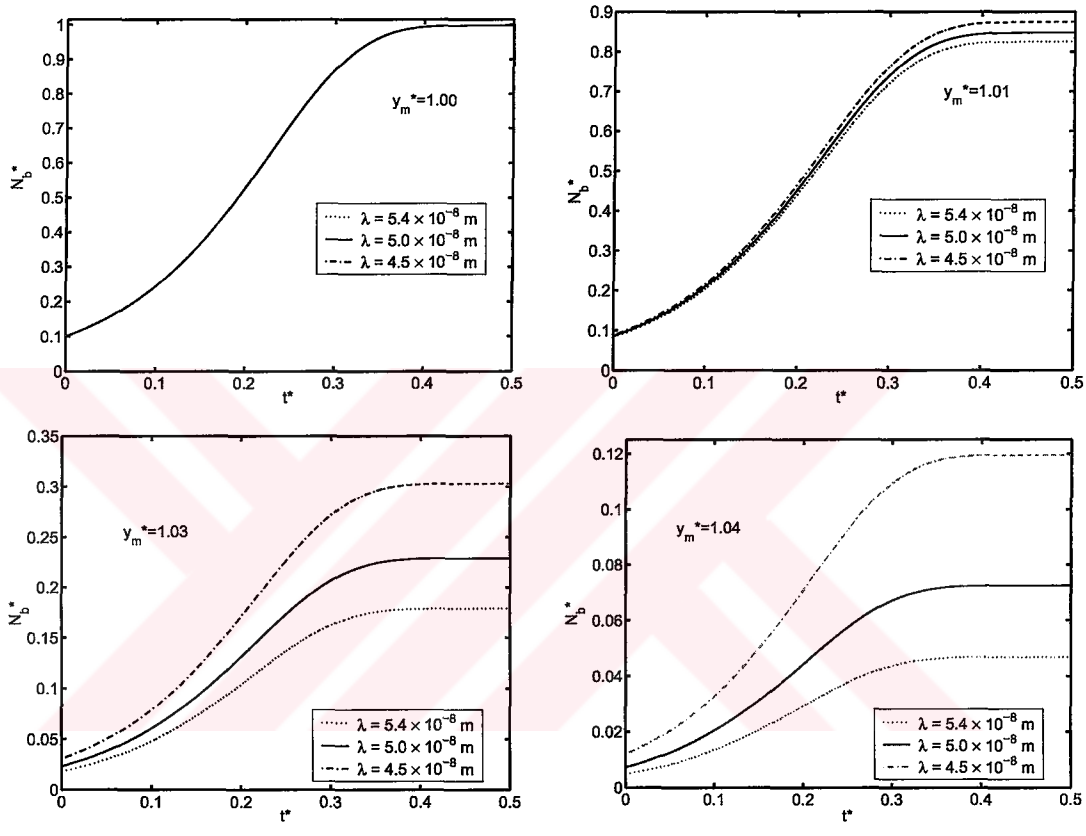

Figure 5.12: Effect of the equilibrium bond length λ on the bond density N_b. The variation of the bond density with time is examined at four different locations (from surface).

Figure 5.12 shows that for a specified time an increase in the equilibrium bond length λ decreases the bond density N_b. Figure 5.13 demonstrates that the bond density N_b reaches a maximum when the vertical distance of the membrane from the substrate surface (y_m) is equal to the equilibrium bond length λ.

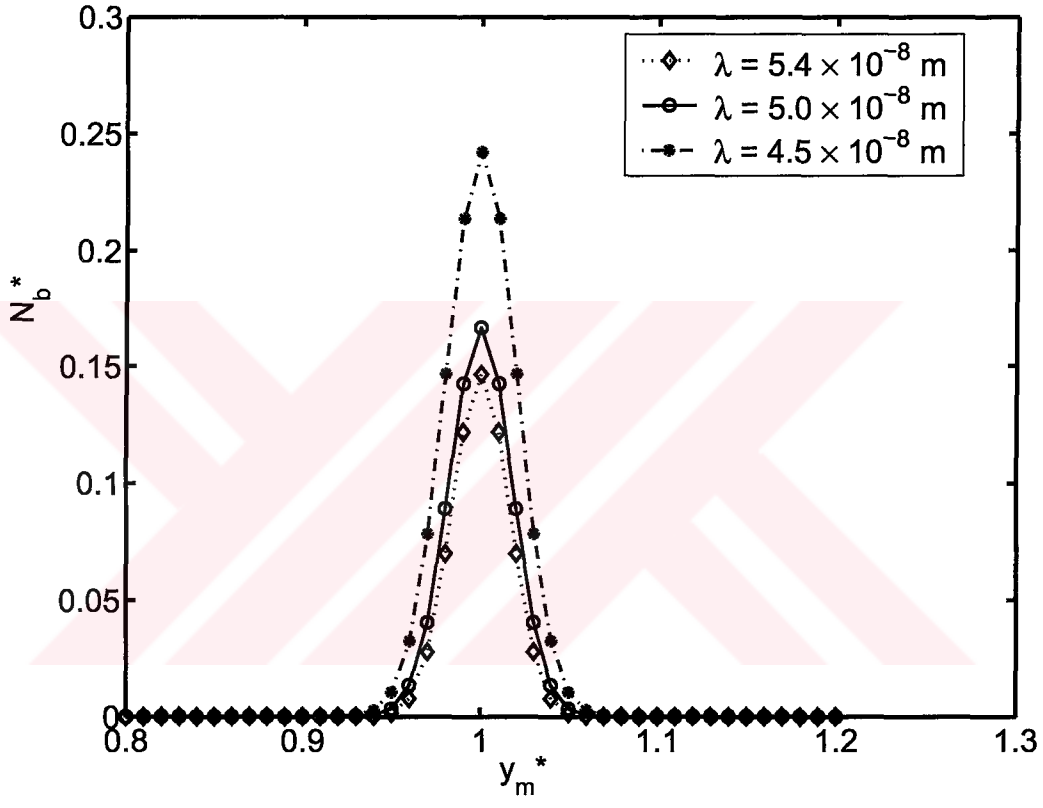

Figure 5.13: Effect of the equilibrium bond length λ on the bond density N_b. The variation of the bond density with the distance from surface is demonstrated.

5.5 Integration of the Kinetic Equation

Since the kinetic equation (Eq.(5.4)) is a very stiff ordinary differential equation, typical integration methods (e.g., Euler Methods, Runge-Kutta Methods and Adams-Bashforth method) have very restrictive constraints on the time step. In order to incorporate the micro-model to the original code, the kinetic equation (Eq.(5.4)) is solved semi-analytically. It is called semi-analytical, because the position of the interface is not computed in the micro-model; it is transmitted from the macro-model. In this section, the development of this semi-analytic method is explained.

The kinetic equation (Eq.(5.4)) can be written as

$$\frac{dN_b}{dt} = k_f(N_l - N_b)(N_r - N_b) - k_r N_b = aN_b{}^2 + bN_b + c \tag{5.8}$$

where

$$\begin{aligned} a &= k_f, \\ b &= -k_f(N_r + N_l) - k_r, \\ c &= k_f N_r N_l. \end{aligned} \tag{5.9}$$

Eq.(5.8) can be written as

$$\frac{dN_b}{dt} = a(N_b - N_1)(N_b - N_2), \tag{5.10}$$

where

$$\begin{aligned} N_1 &= \frac{-b + \sqrt{b^2 - 4ac}}{2a}, \\ N_2 &= \frac{-b - \sqrt{b^2 - 4ac}}{2a}, \end{aligned} \tag{5.11}$$

are the roots of the right hand side of Eq.(5.8). Rearranging and taking the integral of the both sides of the Eq.(5.10) yields

$$\int \frac{dN_b}{(N_b - N_1)(N_b - N_2)} = \int a dt. \tag{5.12}$$

After rearrangement of the left hand side of Eq.(5.12), it becomes

$$\int \left\{ \frac{-\frac{1}{N_2 - N_1}}{N_b - N_1} + \frac{\frac{1}{N_2 - N_1}}{N_b - N_2} \right\} dN_b = \int a dt. \tag{5.13}$$

Integration of the Eq.(5.13) yields

$$\frac{1}{N_2 - N_1}\{-\ln(N_b - N_1) + \ln(N_b - N_2) - \ln C\} = at \tag{5.14}$$

where C is the integration constant.

Eq.(5.14) can be written as

$$\ln \frac{N_b - N_2}{C(N_b - N_1)} = a(N_2 - N_1)t. \tag{5.15}$$

Further simplification of Eq.(5.15) yields

$$\frac{N_b - N_2}{N_b - N_1} = Ce^{a(N_2 - N_1)t}. \tag{5.16}$$

Applying the initial condition

$$N_b \mid_{t=0} = N_{bo}, \tag{5.17}$$

Eq.(5.16) yields

$$\frac{N_{bo} - N_2}{N_{bo} - N_1} = C \tag{5.18}$$

Substitution of $a = k_f$ and Eq.(5.18) into the Eq.(5.16) results in

$$\frac{N_b - N_2}{N_b - N_1} = \frac{N_{bo} - N_2}{N_{bo} - N_1} e^{k_f(N_2 - N_1)t} \tag{5.19}$$

After multiplication of the both sides of the Eq.(5.19) with $(N_b - N_1)$, it becomes

$$N_b - N_2 = \frac{N_{bo} - N_2}{N_{bo} - N_1}(N_b - N_1)e^{k_f(N_2 - N_1)t}, \tag{5.20}$$

which can be written as

$$N_b - \frac{N_{bo} - N_2}{N_{bo} - N_1}(N_b)e^{k_f(N_2 - N_1)t} = N_2 - \frac{N_{bo} - N_2}{N_{bo} - N_1}(N_1)e^{k_f(N_2 - N_1)t}, \tag{5.21}$$

Rearrangement of the Eq.(5.21) yields

$$N_b = \frac{N_2 - \frac{N_{bo} - N_2}{N_{bo} - N_1}(N_1)e^{k_f(N_2 - N_1)t}}{1 - \frac{N_{bo} - N_2}{N_{bo} - N_1}e^{k_f(N_2 - N_1)t}}. \tag{5.22}$$

Now, the exponential coefficient in the Eq.(5.22) can be written as

$$\begin{aligned} k_f(N_2 - N_1) &= k_f\left\{\frac{-b - \sqrt{b^2 - 4ac}}{2a} - \frac{-b + \sqrt{b^2 - 4ac}}{2a}\right\} \\ &= k_f\left\{\frac{-\sqrt{b^2 - 4ac}}{k_f}\right\} \\ &= -\sqrt{b^2 - 4ac} \end{aligned} \tag{5.23}$$

or

$$k_f(N_2 - N_1) = -\left\{\sqrt{\left(\frac{b}{a}\right)^2 - 4\left(\frac{c}{a}\right)}\right\} k_f. \tag{5.24}$$

Rearranging the Eq.(5.11) yields

$$\begin{aligned} N_1 &= \frac{1}{2}\left\{-\frac{b}{a} + \sqrt{\left(\frac{b}{a}\right)^2 - 4\left(\frac{c}{a}\right)}\right\} = \frac{1}{2}\left\{-\frac{b}{a} + \sqrt{\Delta}\right\} \\ N_2 &= \frac{1}{2}\left\{-\frac{b}{a} - \sqrt{\left(\frac{b}{a}\right)^2 - 4\left(\frac{c}{a}\right)}\right\} = \frac{1}{2}\left\{-\frac{b}{a} - \sqrt{\Delta}\right\} \end{aligned} \tag{5.25}$$

where

$$\begin{aligned} \Delta &= \left(\frac{b}{a}\right)^2 - 4\left(\frac{c}{a}\right) = \left[\frac{-k_f(N_l + N_r) - k_r}{k_f}\right]^2 - 4\left[\frac{k_f N_r N_l}{k_f}\right] \\ &= \left[(N_l + N_r) + \frac{k_r}{k_f}\right]^2 - 4N_r N_l \\ &= (N_r + N_l)^2 + 2\frac{k_r}{k_f}(N_r + N_l) + \left(\frac{k_r}{k_f}\right)^2 - 4N_r N_l \\ &= (N_r - N_l)^2 + 2\frac{k_r}{k_f}(N_r + N_l) + \left(\frac{k_r}{k_f}\right)^2 > 0 \end{aligned} \tag{5.26}$$

Numerically more stable form of the Eq.(5.26) can be written as

$$\Delta = {N_l}^2\left[\left\{1 + \frac{N_r}{N_l} + \frac{k_r}{N_l k_f}\right\}^2 - 4\frac{N_r}{N_l}\right]. \tag{5.27}$$

Using the definitions in Eq.(5.9, the term $\left(-\frac{b}{a}\right)$ can be written as

$$-\frac{b}{a} = \frac{k_f(N_r + N_l) + k_r}{k_f} = N_r + N_l + \frac{k_r}{k_f} = N_l\left(1 + \frac{N_r}{N_l} + \frac{k_r}{k_f N_l}\right). \tag{5.28}$$

Substitution of Eq.(5.27) and Eq.(5.28) into Eq.(5.25) yields

$$\begin{aligned} N_1 &= \frac{N_l}{2}\left\{1 + \frac{N_r}{N_l} + \frac{k_r}{k_f N_l} + \sqrt{\left(1 + \frac{N_r}{N_l} + \frac{k_r}{k_f N_l}\right)^2 - 4\frac{N_r}{N_l}}\right\} \\ N_2 &= \frac{N_l}{2}\left\{1 + \frac{N_r}{N_l} + \frac{k_r}{k_f N_l} - \sqrt{\left(1 + \frac{N_r}{N_l} + \frac{k_r}{k_f N_l}\right)^2 - 4\frac{N_r}{N_l}}\right\} \end{aligned} \tag{5.29}$$

In order to simplify the Eq.(5.22) some additional parameters are defined as

$$\alpha_1 = \frac{N_r}{N_l} \tag{5.30}$$

$$\alpha_2 = \frac{k_r}{k_f N_l} \tag{5.31}$$

$$\beta_1 = 1 + \alpha_1 + \alpha_2 \tag{5.32}$$

$$\beta_2 = \sqrt{\beta_1^2 - 4\alpha_1} \tag{5.33}$$

$$\frac{1}{\tau} = k_f(N_2 - N_1). \tag{5.34}$$

Using the definitions in Eq.(5.6) and Eq.(5.5), Eq.(5.31) can be written as

$$\alpha_2 = \frac{k_r}{k_f N_l} = \frac{k_{ro}}{k_{fo} N_l} \exp \frac{\sigma(y_m - \lambda)^2}{2k_b T}. \tag{5.35}$$

Eq.(5.29) can also be written as

$$\begin{aligned} N_1 &= \frac{1}{2} N_l(\beta_1 + \beta_2) \\ N_2 &= \frac{1}{2} N_l(\beta_1 - \beta_2). \end{aligned} \tag{5.36}$$

Rearrangement of Eq.(5.34) yields

$$\begin{aligned} \frac{1}{\tau} &= k_f(N_2 - N_1) = k_f \sqrt{\left(\frac{b}{a}\right)^2 - 4\left(\frac{c}{a}\right)} \\ &= k_f N_l \sqrt{\left\{1 + \frac{N_r}{N_l} + \frac{k_r}{N_l k_f}\right\}^2 - 4\frac{N_r}{N_l}} \\ &= k_f N_l \beta_2 \\ &= \beta_2 k_f o N_l \exp \frac{-\sigma_t s(y_m - \lambda)^2}{2k_b T}. \end{aligned} \tag{5.37}$$

In summary, the integration procedure of the kinetic equation (Eq.(5.4)) can be given as

$$\begin{aligned} N_{bo} &= N_b^n \\ N_b &= N_b^{n+1} \\ N_b^{n+1} &= \frac{N_2 - \frac{N_{bn} - N_2}{N_{bn} - N_1}(N_1) e^{\frac{-\delta t}{\tau}}}{1 - \frac{N_{bn} - N_2}{N_{bn} - N_1} e^{\frac{-\delta t}{\tau}}} \end{aligned} \tag{5.38}$$

where n is the time level.

5.6 Coupling of the Micro- and Macro-Models

At each time step, the location of the interface is determined by solving the macro-model while freezing the micro-model. The information concerning about the location of the interface is transmitted to the micro-model where the total bond force F_b is computed. Then, this total bond force is transmitted to the macro-model via the source term as shown in Eq.(5.1). During the course of the computation, information between the macro- and micro models is continuously exchanged.

5.7 Results and Discussion

In this section, cell detachment and rolling cases are simulated using the leukocyte model which includes the linear springs between the nucleus and cortex. Furthermore, the effect of the parameter γ which is the ratio of the spring to the surface tension forces (as explained in Appendix A) on the rolling process is investigated. In all the simulations, parameters on the order of those estimated for the leukocytes are used. The radius of the leukocyte is set to 4 μm, and the radius of the nucleus is set to 2.5 μm. The computational domain which represents a narrow vessel is a rectangle with 64x10^{-6} m in length and 16x10^{-6} m in width which is resolved by a 256x64 grid. It is assumed that the bottom side of the domain is coated with ligands. In the beginning of the simulations, the leukocyte is placed close to the bottom side of the domain, and a shear flow is applied at the entrance (left hand side of the domain) of the channel. All simulations in this chapter are performed at a constant wall shear rate of 250 s^{-1}, which is in the range for which leukocyte rolling is observed [45].

5.7.1 Representative Simulation of Leukocyte Detachment and Rolling

In this section, detachment and subsequent rolling events of the leukocyte are simulated. The mechanical and kinetic parameters used in the simulations are shown in Table 5.3 and Table 5.4, respectively. Initially, the leukocyte is placed close to the bottom side of the domain so that the distance between them is 25 μm. Then, a shear flow is imposed at the inlet (left hand side) of the computational domain.

Figure 5.16 shows the evolution of the shapes of the leukocyte model. As seen in Fig. 5.16, initially, the adhesive forces between surface ligands and cell receptors are dominant, and

Mechanical parameter	**Value used in simulation**
Surface tension (outer membrane)	$4 \times 10^{-5}\ N/m$
Surface tension (inner membrane)	$10^{-4}\ N/m$
Viscosity (surrounding fluid)	$0.1\ Ns/m^2$
Viscosity (cytoplasm)	$10\ Ns/m^2$
Viscosity (nucleus)	$100\ Ns/m^2$
Density (surrounding fluid)	$10^7\ kg/m^3$
Density (cytoplasm)	$10^9\ kg/m^3$
Density (nucleus)	$10^{10}\ kg/m^3$
(inner spring forces)/(surface tension forces)	1

Table 5.3: The mechanical parameters used in the simulation of leukocyte rolling.

Kinetic parameter	**Value used in simulation**
N_r	$5.0 \times 10^{14}\ m^{-2}$
N_l	$5.0 \times 10^{14}\ m^{-2}$
k_{fo}	$10^{-10}\ m^2 s^{-1}$
k_{ro}	$0.1\ s^{-1}$
σ_s	$1.00 \times 10^{-6}\ N/m$
σ_{ts}	$0.99 \times 10^{-6}\ N/m$
λ	$50 \times 10^{-8}\ m$
k_bT	$4.1 \times 10^{-21}\ Joule$

Table 5.4: Kinetic parameters used in the simulation of leukocyte rolling.

the leukocyte seems to be attached to the surface. With increasing time, the hydrodynamic forces which result from the shear flow gain the control, and the detachment and subsequent rolling of the leukocyte is observed. In the recent simulations of N'dri et al. [43], they observed that the shape of cell became nonphysical when the cell traveled more than two cell radii. In the present study, the leukocyte rolls without a nonphysical change in its shape.

Figure 5.15 shows the force vectors due to the adhesion forces and inner spring forces. The line segments between the cortex and nucleus represent the inner springs, and are virtual. They are drawn in order to describe the leukocyte model clearly. In Fig. 5.15(a), the attractive and repulsive forces due to the kinetic model of Dembo [2] are demonstrated. Since the equilibrium bond length is 50 μm, the part of the leukocyte which lies closer than 50 μm to the surface is exposed to repulsive forces. For the other parts of the leukocyte, which lie far away from the surface than 50 μm, the bond density is computed. The parts which have a bond density less than a critical value (in this work, it is 10^{-4} times the equilibrium bond density), are not exposed to adhesive forces, whereas the others are pulled towards the surface. Figure 5.15(b) shows the inner spring forces and adhesion forces. During the detachment phase, the hydrodynamic forces (due to the shear flow) overcome the adhesive forces and the leukocyte begins to move and deform. Since linear springs exist between the nucleus and cortex, repulsive and attractive forces are created in order to maintain the original shape. The nucleus and cortex apply repulsive forces to each other when they are closer to each other than the original distance; and they apply attractive forces to each other when they are far away from each other than the original distance.

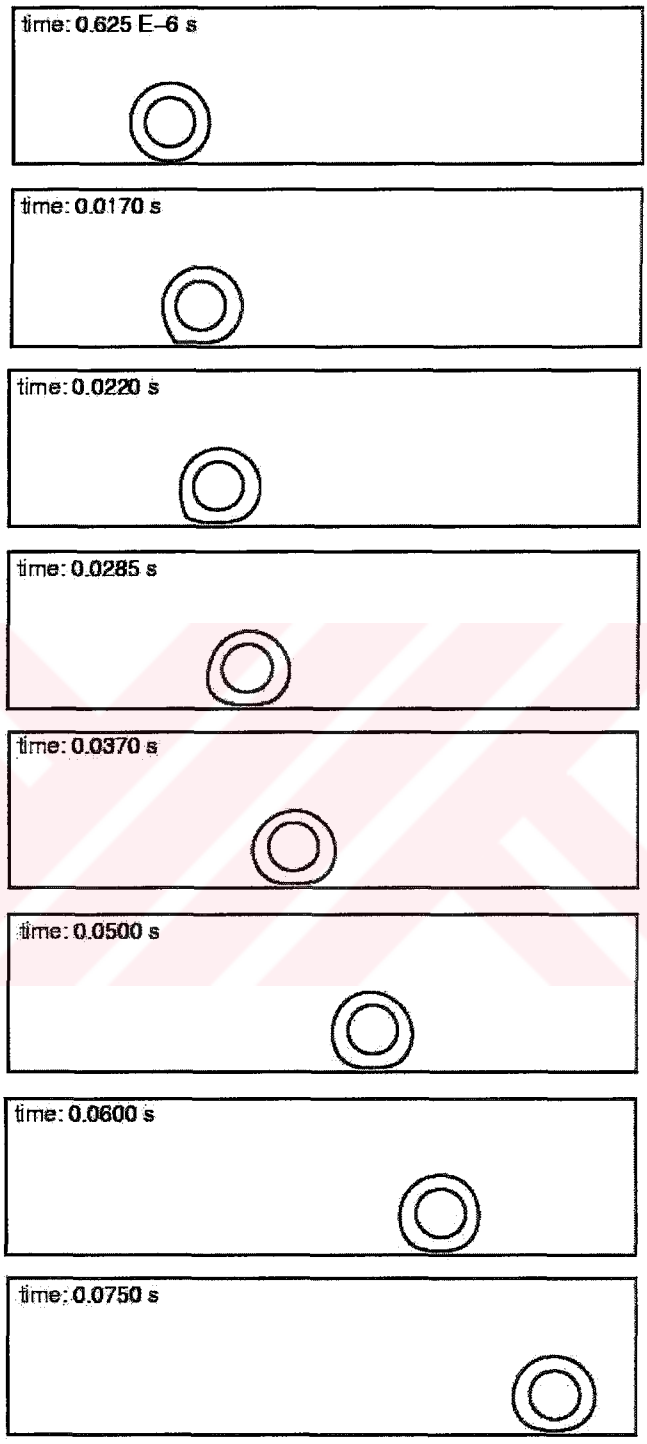

Figure 5.14: Evolution of the shape of the leukocyte during the detachment and rolling events

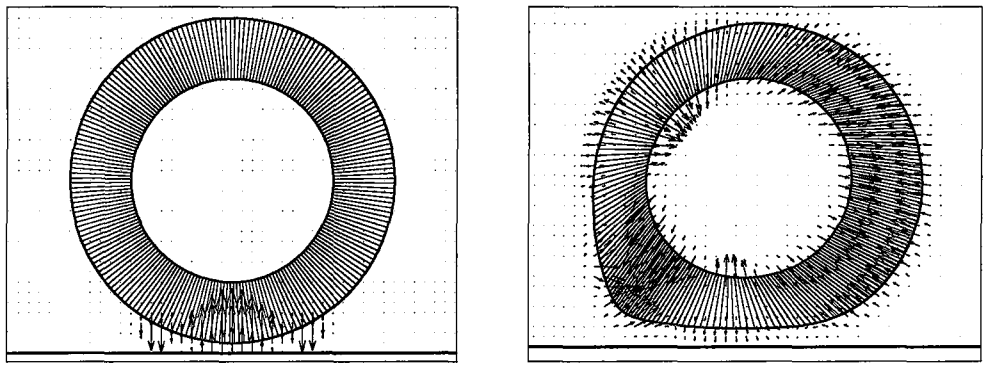

(a) (b)

Figure 5.15: The representation of the adhesion and inner spring forces: (a) Attractive and repulsive forces due to the kinetic model of Dembo [2] at time frame: 0.000000625 s. (b) The inner spring forces and adhesion forces at time frame: 0.0220 s.

5.7.2 Effect of The Parameter γ on Leukocyte Rolling

In this section, the effect of the parameter γ which is the ratio of the spring to the surface tension forces (as explained in Appendix A) on the leukocyte rolling process is investigated. The mechanical and kinetic parameters used in the simulations are the same as in section 5.7.1, except the parameter γ. Initially, the leukocyte is placed close to the bottom side of the domain so that the distance between them is 25 μm. Then, a shear flow is imposed at the inlet (left hand side) of the computational domain. The detachment and rolling of leukocyte is analyzed for three different values of the parameter γ. Figure 5.15 shows that for the same time frame, the leukocyte rolls faster with increasing values of γ. This is reasonable, since greater γ values result in a faster recovery of the deformed leukocyte to its original shape, which decreases the contact area of the leukocyte with the surface. A decrease in the contact area between the leukocyte and the surface results in a decrease in adhesive forces, which accelerates the detachment and subsequent rolling of the leukocyte.

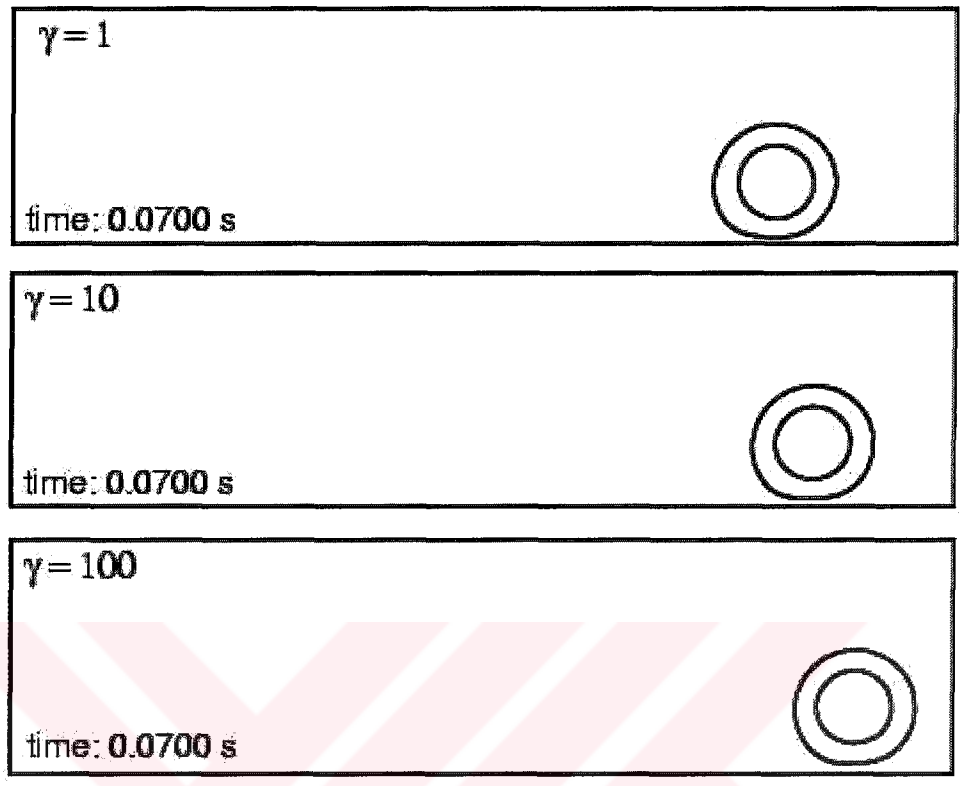

Figure 5.16: Effect of the parameter γ on leukocyte detachment and rolling events.

Chapter 6

CONCLUSIONS

In this study, the leukocyte is modeled as a viscous fluid that moves in a surrounding less viscous fluid. The dynamics of large-scale deformations of the leukocytes in a given flow field is investigated within the framework of finite-difference/front-tracking methodology.

In chapter 4, simulations of cell-entry micro-pipette experiments have been presented in order to demonstrate the capabilities of the method. The evolution of the shape of the leukocyte as it enters the micro-pipette, as well as the rate of entry of the leukocyte into the micro-pipette are compared qualitatively with experimental findings. Preliminary comparisons using a model of a Newtonian drop for the mechanics of the leukocytes show a similar trend in the effects of the suction pressure on the rate of entry of leukocytes between the simulations and the experiments so that an increase in suction pressure from 1 to 2 kPa increases the rate of entry by about factor of two. The absolute rate of entry is slower in the simulations than observed in the experiments, and possible reasons for this discrepancy were discussed.

In addition to the simple drop model (Model 1), two different models for the mechanics of leukocytes have also been analyzed. These models are namely a Newtonian fluid including a more viscous nucleus inside (Model 2), and a Newtonian fluid with a more viscous nucleus which includes liner springs between the outer and inner membranes (Model 3). Model 3 allows both co-centric and off-centric configurations of the nucleus and cortex; and it is fully reversible, i.e., the cell restores to its initial undeformed configuration when the external forces are removed. It is found that the different models affect both the shape and the rate of entry of leukocytes into the micro-pipette. The presence of a more viscous nucleus increased the rate of entry of the leukocyte into the micro-pipette; and this behavior agrees qualitatively with the experimental observations for leukocytes [42], but the characteristics of the projection length vs time curves for Model 2 and Model 3 are different from that observed in the micro-pipette experiments.

In chapter 5, a multi-scale model similar to that of the N'Dri et al. [43] is used for the analysis of adhesion dynamics of leukocytes. The multi-scale model is composed of two parts: the micro-model and the macro-model. The macroscopic part dealt with the deformation of the leukocyte and the microscopic part accounted for the adhesion process. In this chapter, cell detachment and rolling cases are simulated using the leukocyte model which includes the linear springs between the nucleus and cortex. Furthermore, the effect of the parameter γ which is the ratio of the spring to the surface tension forces (as explained in Appendix A) on the rolling process is investigated. It is found that the leukocyte rolls faster with increasing values of γ.

In this work, the kinetic model proposed by Dembo et al. [2] is used, and the and the effect of nonspecific forces is neglected. In addition, it is assumed that the bond molecules are fixed on the membrane surface, which is not the case because bond molecules have shown to diffuse laterally to the contact area [26].

Improvement of the model for the mechanics of the deformation of leukocytes requires extension to the three dimensional or axis-symmetric computational domain, incorporating and testing a range of possible parameters (e.g. a more detailed representation of the microtubles and micro filaments, addition of the nonspecific forces), and simulating various experimental setups. A more detailed three dimensional or antisymmetric model of leukocyte is left for future work.

Appendix A

CELL SQUEEZING

In this section, an analysis based on the cell squeezing is presented for the cell model presented in section 4.1. The cell squeezing and cell poking are used to determine the mechanical properties of biological cells [46] along with the micro-pipette aspiration [47]. It has been demonstrated by Zahalak et al. [46] that cell poking gives more complete information about properties of the cell mechanics than the micro-pipette aspiration experiments. Figure A.1 shows a sketch of a typical cell poker. In this experiment, the cell is squeezed by two parallel plates and the reaction force acting on the poker surface is measured.

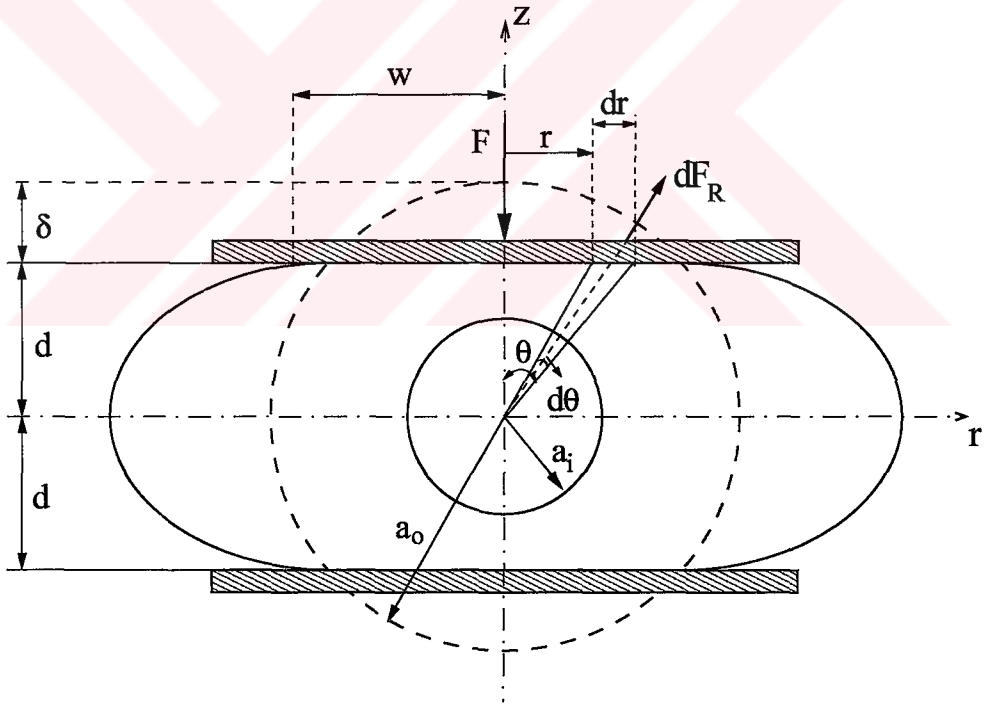

Figure A.1: Sketch of the Cell Poker.

In the sketch in Fig. A.1, a_o and a_i denote the radius of the undeformed cell and the

radius of the nucleus respectively. In the present analysis, the problem is assumed to be axisymmetric. The radial and axial coordinates are denoted by r and z, respectively. The total force acting on the plate and the indentation are denoted by F and δ, respectively. It is also assumed that the nucleus is rigid and the orientation of the linear springs connecting the nucleus and the cortex is such that their axes pass through the origin during and after the squeezing.

The total force acting on the cell poker in the normal direction can be written as

$$F = F_{spring} + F_{pressure}, \tag{A.1}$$

where F_{spring} and $F_{pressure}$ denote the forces due to the springs and due to the pressure difference between inside and outside of cell cortex, respectively.

Referring to the sketch in Fig. A.1, the reaction force acting on the differential surface area element ds of cell poker due to springs in the normal direction is given by

$$dF_{spring} = dF_{R_{spring}} \cos\theta = (k\Delta l ds)\cos\theta \tag{A.2}$$

where k is the spring coefficient. Based on the assumptions mentioned above, one can write

$$\begin{aligned} \Delta l &= a_o - \sqrt{d^2 + r^2}, \\ ds &= 2\pi r dr, \\ d &= a_o - \delta, \\ \cos\theta &= \frac{a_o - \delta}{\sqrt{(a_o - \delta)^2 + r^2}}. \end{aligned} \tag{A.3}$$

Substituting Eqs.(A.3) into Eq.(A.2) yields

$$dF_{spring} = 2\pi k(a_o - \delta)\left[\frac{a_o r}{\sqrt{(a_o - d)^2 + r^2}} - r\right] dr \tag{A.4}$$

which can be integrated over the cell poker surface to obtain

$$\begin{aligned} F_{spring} &= 2\pi k(a_o - \delta)\left\{a_o \int_0^w \frac{r}{\sqrt{(a_o - d)^2 + r^2}} dr - \int_0^w r dr\right\} \\ &= 2\pi k(a_o - \delta)\left\{a_o\sqrt{(a_o - \delta)^2 + w^2} - \frac{1}{2}w^2 - a_o(a_o - \delta)\right\}. \end{aligned} \tag{A.5}$$

where w denotes the radius of the portion of cell poker that is in touch with the cell as shown in the sketch (see the Fig. A.1). Equation (A.5) can be rearranged to get

$$F_{spring} = 2\pi k a_o^2(a_o - \delta)\left\{\sqrt{\left(1 - \frac{\delta}{a_o}\right)^2 + \left(\frac{w}{a_o}\right)^2} - \frac{1}{2}\left(\frac{w}{a_o}\right)^2 - \left(1 - \frac{\delta}{a_o}\right)\right\} \tag{A.6}$$

The force due to pressure difference is given by

$$F_{pressure} = \pi w^2 \Delta p, \tag{A.7}$$

where Δp is the pressure difference inside and outside of the cell. Thus Eq.(A.1) becomes

$$F = 2\pi k a_o^2 (a_o - \delta) \left\{ \sqrt{\left(1 - \frac{\delta}{a_o}\right)^2 + \left(\frac{w}{a_o}\right)^2} - \frac{1}{2}\left(\frac{w}{a_o}\right)^2 - \left(1 - \frac{\delta}{a_o}\right) \right\} + \pi w^2 \Delta p. \tag{A.8}$$

To compute the pressure difference Δp, the shape of the cross-section of the portion of the cell outside of the cell poker is approximated as a half ellipse. Referring to the sketch in Fig. A.2, the curve ABC is assumed to be elliptical and is given by

$$\frac{(r-w)^2}{f^2} + \frac{z^2}{d^2} = 1, \tag{A.9}$$

where f and d are semi axes. Then the principal radii of curvature at points A and B in the sketch are given by

$$\begin{aligned} R_{A_1} &= \frac{d^2}{f}; \quad R_{A_2} = w + f \\ R_B &= R_{B_1} = R_{B_2} = \frac{f^2}{d}. \end{aligned} \tag{A.10}$$

The spring force acting at the point B in the normal direction (per unit area) is given by

$$f_{B_{spring}} = k(|OB| - a_o)\sin\phi = k\left(\sqrt{d^2 + w^2} - a_o\right)\frac{d}{\sqrt{d^2 + w^2}} \tag{A.11}$$

or

$$f_{B_{spring}} = kd\left(1 - \frac{a_o}{\sqrt{(a_o - \delta)^2 + w^2}}\right) \tag{A.12}$$

On the other hand, the force due to surface tension in the normal direction at point B is given by

$$f_{B_{surface}} = \sigma\left(\frac{1}{R_{B_1}} + \frac{1}{R_{B_2}}\right) = \frac{2\sigma(a_o - \delta)}{f^2}, \tag{A.13}$$

where σ is the surface tension coefficient of the outer membrane (cortex). Thus the pressure jump at point B is given by

$$\Delta p_B = \frac{2\sigma(a_o - \delta)}{f^2} + k(a_o - \delta)\left(1 - \frac{a_o}{\sqrt{(a_o - \delta)^2 + w^2}}\right). \tag{A.14}$$

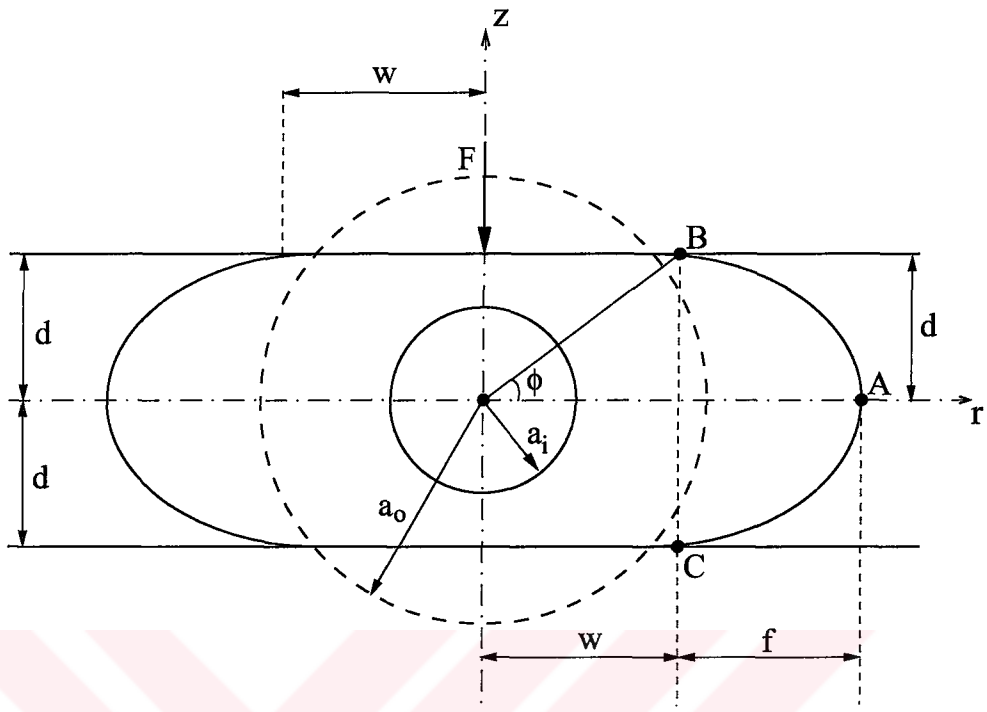

Figure A.2: Sketch of the Cell Poker. It is assumed that ABC is half of the ellipse.

Similarly, the pressure jump at point A is

$$\Delta p_A = f_{A_{surface}} + f_{A_{spring}} \tag{A.15}$$

where

$$f_{A_{surface}} = \sigma \left(\frac{1}{R_{A_1}} + \frac{1}{R_{A_2}} \right) = \sigma \left(\frac{f}{(a_o - \delta)^2} + \frac{1}{w + f} \right). \tag{A.16}$$

and

$$f_{A_{spring}} = k(|OA| - a_o) = k(w + f - a_o). \tag{A.17}$$

Thus

$$\Delta p_A = \sigma \left(\frac{f}{(a_o - \delta)^2} + \frac{1}{w + f} \right) + k(w + f - a_o). \tag{A.18}$$

Since the pressure jumps at both points must be equal in equilibrium, we have from

Eqs.(A.14) and (A.18)

$$\sigma\left(\frac{f}{(a_o-\delta)^2}+\frac{1}{w+f}\right)+k(w+f-a_o)= \frac{2\sigma(a_o-\delta)}{f^2}+k(a_o-\delta)\left(1-\frac{a_o}{\sqrt{(a_o-\delta)^2+w^2}}\right), \tag{A.19}$$

which can be rearranged as

$$\frac{1}{f^2}-\frac{1}{2}\left[\frac{1}{(a_o-\delta)^3}+\frac{k}{\sigma(a_o-\delta)}\right]f-\frac{1}{2(a_o-\delta)(w+f)}= \frac{k}{2\sigma(a_o-\delta)}\left[w+\delta-2a_o+\frac{a_o(a_o-\delta)}{\sqrt{(a_o-\delta)^2+w^2}}\right]. \tag{A.20}$$

Let

$$f^*=\frac{f}{a_o};\quad \delta^*=\frac{\delta}{a_o};\quad w^*=\frac{w}{a_o}, \tag{A.21}$$

then Eq.(A.20) can be written in non-dimensional form as

$$\frac{1}{f^{*2}}-\frac{1}{2}\left[\frac{1}{(1-\delta^*)^3}+\frac{\gamma}{(1-\delta^*)}\right]f^*-\frac{1}{2(1-\delta^*)(w^*+f^*)}= \frac{\gamma}{2(1-\delta^*)}\left[w^*+\delta^*-2+\frac{(1-\delta^*)}{\sqrt{(1-\delta^*)^2+w^{*2}}}\right], \tag{A.22}$$

where

$$\gamma=\frac{ka_o^2}{\sigma} \tag{A.23}$$

represents the ratio of the spring to the surface tension forces. Eq.(A.22) can be written as

$$\frac{1}{f^{*2}}-\alpha f^*-\frac{\eta}{w^*+f^*}=\beta \tag{A.24}$$

where

$$\begin{aligned}\alpha &= \frac{1}{2}\left[\frac{1}{(1-\delta^*)^3}+\frac{\gamma}{(1-\delta^*)}\right]\\ \eta &= \frac{1}{2}\frac{1}{1-\delta^*}\\ \beta &= \frac{\gamma}{2(1-\delta^*)}\left[w^*+\delta^*-2+\frac{(1-\delta^*)}{\sqrt{(1-\delta^*)^2+w^{*2}}}\right].\end{aligned} \tag{A.25}$$

Equation (A.24) can be rearranged as

$$\alpha f^{*3}-\eta\frac{f^{*2}}{w^*+f^*}+\beta f^{*2}-1=0. \tag{A.26}$$

In Eq.(A.24), both f^* and w^* are unknown so that we need one more equation to solve for these unknowns. The second equation is obtained from the mass conservation, i.e,

$$\begin{aligned} V = \frac{4}{3}\pi a_o^3 &= 2\pi \int_0^d r^2 dz \\ &= 2\pi \int_0^d \left[w + f\sqrt{\left(1 - \frac{z^2}{d^2}\right)} \right]^2 dz \\ &= 2\pi d \left[w^2 + \frac{\pi}{2} wf + \frac{2}{3} f^2 \right], \end{aligned} \tag{A.27}$$

which can be rearranged to obtain

$$f^2 + \frac{3}{4}\pi w f + \frac{3}{2} w^2 - \frac{a_o^3}{a_o - \delta} = 0 \tag{A.28}$$

or in non-dimensional form

$$w^{*2} + \frac{8\pi}{9} f^* w^* + \frac{2}{3} f^{*2} - \frac{2}{3}\frac{1}{1-\delta^*} = 0. \tag{A.29}$$

In summary, the equations to be solved are

$$\begin{aligned} w^2 &+ \frac{8\pi}{9} fw + \frac{2}{3} f^2 - \frac{2}{3}\frac{1}{1-\delta} = 0 \\ \alpha f^3 &- \eta \frac{f^2}{w+f} + \beta f^2 - 1 = 0 \\ \alpha &= \frac{1}{2}\left[\frac{1}{(1-\delta^*)^3} + \frac{\gamma}{(1-\delta^*)} \right] \\ \eta &= \frac{1}{2}\frac{1}{1-\delta^*} \\ \beta &= \frac{\gamma}{2(1-\delta^*)} \left[w^* + \delta^* - 2 + \frac{(1-\delta^*)}{\sqrt{(1-\delta^*)^2 + w^{*2}}} \right] \\ \gamma &= \frac{k a_o^2}{\sigma}. \end{aligned} \tag{A.30}$$

Equations (A.30) are solved numerically to obtain f^* and w^* for given non-dimensional indentation δ^*. Then the non-dimensional reaction force exerted on the poker surface is

$$F^* = F^*_{spring} + F^*_{pressure} \tag{A.31}$$

where

$$F^* = \frac{F}{2\pi a_o \sigma} \tag{A.32}$$

and

$$\begin{aligned} F^*_{spring} &= \frac{F_{spring}}{2\pi a_o \sigma} = \gamma(1-\delta^*)\left\{\sqrt{(1-\delta^*)^2+w^{*2}} - \frac{1}{2}w^{*2} - (1-\delta^*)\right\} \\ F^*_{pressure} &= \frac{F_{pressure}}{2\pi a_o \sigma} = w^{*2}\frac{\Delta p}{2\sigma}a_o \\ &= \left[\frac{1-\delta^*}{f^{*2}} + \gamma\frac{1-\delta^*}{2}\left(1 - \frac{1}{\sqrt{(1-\delta^*)^2+w^{*2}}}\right)\right]w^{*2}. \end{aligned} \tag{A.33}$$

For the various values of the parameter γ which represents the ratio of the spring to the surface tension forces, total force F^* versus indentation δ^*, the ratio of the pressure force to the total force $F^*_{pressure}/F^*$ versus δ^*, horizontal radius f^* versus δ^* and w^* versus δ^* plots are demonstrated in Fig. A.3, Fig. A.4, Fig. A.5 and Fig. A.6, respectively.

Figure A.3 shows that for a specified value of indentation δ^*, the total force increases with increasing γ. This is physically obvious, since more force should be exerted on the plate of the cell poker in order to squeeze a cell which contains stiffer springs between the nucleus and the cortex. In the same figure, it can be seen that the total force increases with increasing indentation. This is true, since one needs to exert more force in order to increase the indentation.

In Fig. A.4 it is demonstrated that an increase in γ decreases the ratio of the pressure force to the total force. Since the total force is composed of the spring and pressure forces, and an increase in γ means an increase in the spring force (and also an increase in the total force), the ratio of the pressure force to the total force decreases when γ decreases. In the same figure, for the case when $\gamma = 0$, the ratio of the pressure force to the total force does not change with indentation since $\gamma = 0$ means that the spring force is zero and the pressure force is equal to the total force.

Figure A.5 shows that f^* decreases with increasing γ and increasing indentation.

In Figure.A.6 it is demonstrated that w^* increases with increasing γ and increasing indentation.

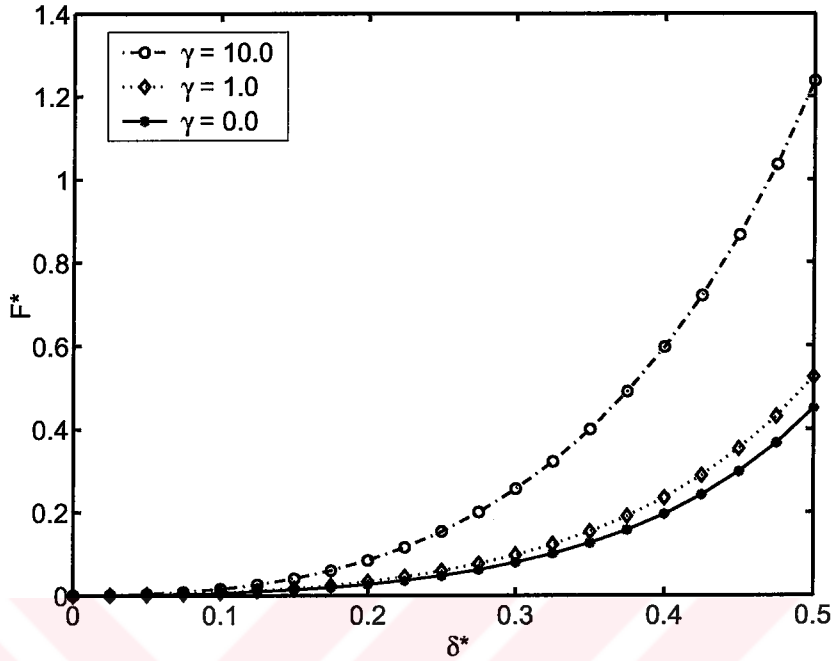

Figure A.3: Total force F^* versus δ^*.

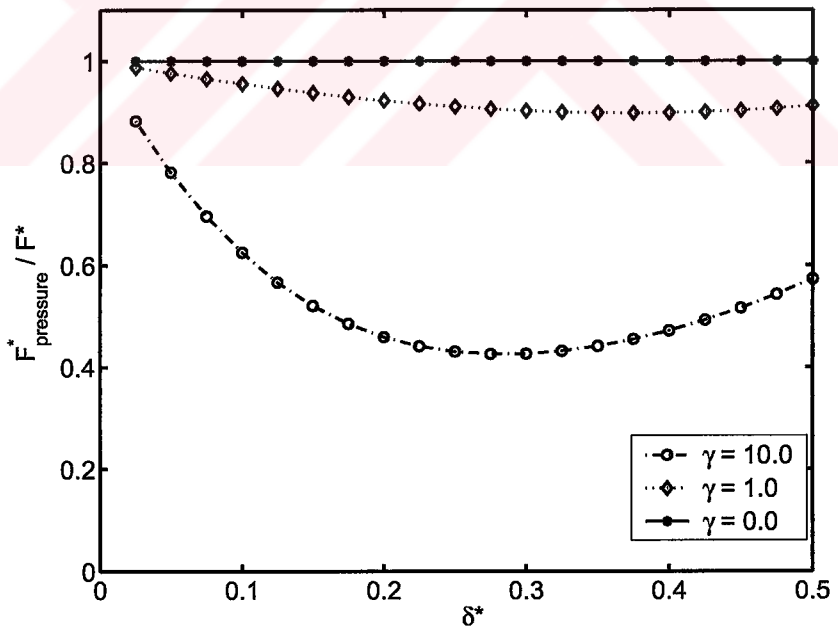

Figure A.4: The ratio of the pressure force to the total force $F^*_{pressure}/F^*$ versus δ^*

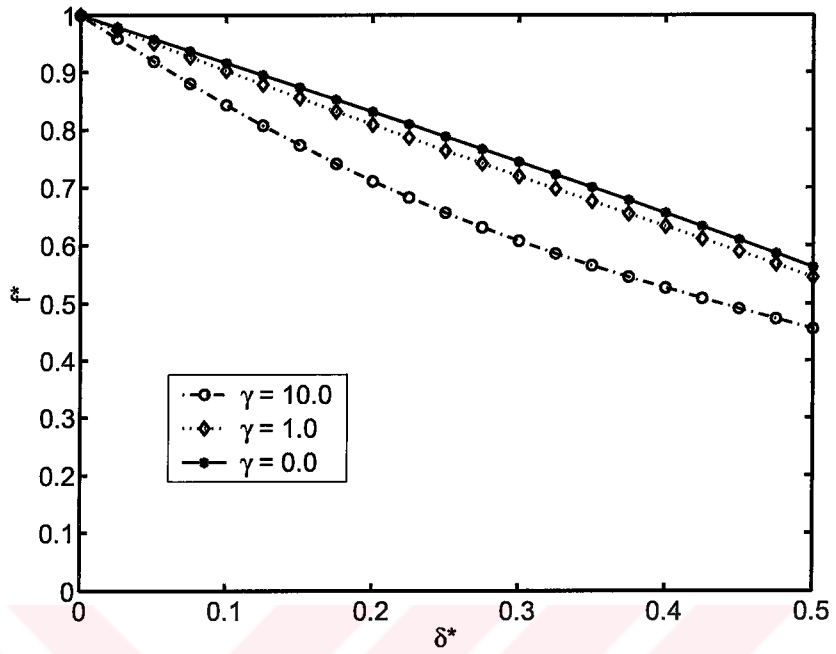

Figure A.5: Horizontal radius f^* versus δ^*

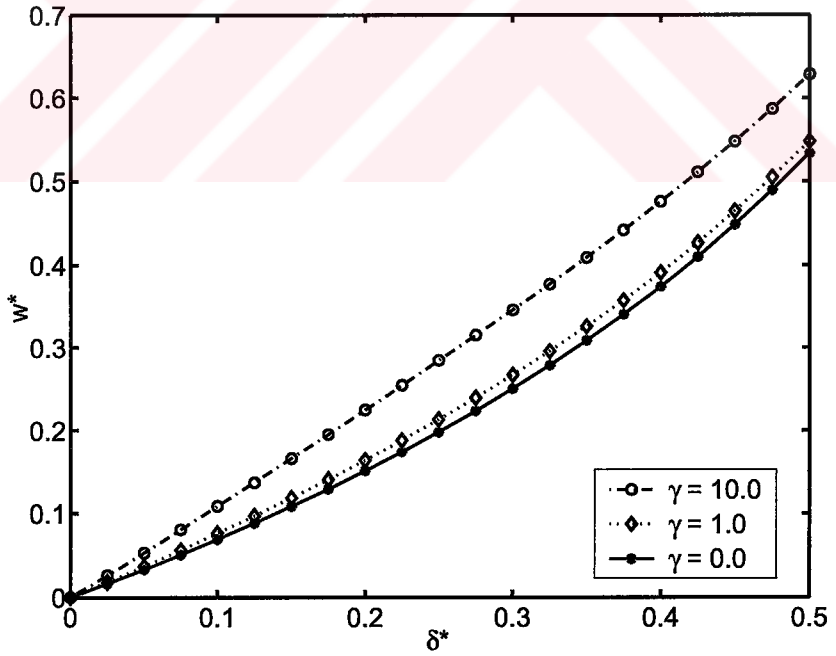

Figure A.6: w^* versus δ^*

BIBLIOGRAPHY

[1] H. A. Glossary., "Leukocyte," *http://www.hon.ch/Library/Theme/Allergy/Glossary/wbc.html*, 2002.

[2] M. Dembo, D. Torney, K. Saxman, and D. Hammer, "The reaction-limited kinetics of membrane-to-surface adhesion and detachment," in *Proceedings of the Royal Society of London. Series B, Biological Sciences*, vol. 234, 1988, pp. 55–83.

[3] G. W. Schmidt-Schonbein, K. L. Sung, H.Tozoren, R. Skalak, and S. Chien, "Passive mechanical properties of human leukocytes," *Biophysical Journal*, vol. 36, pp. 243–256, 1981.

[4] G. W. Schmidt-Schonbein, Y. Y. Shih, and S. Chien, "Morphometry of human leukocytes," *Blood*, vol. 56, pp. 886–875, 1980.

[5] S. V. Marella and H. S. Udaykumar, "Computational analysis of the deformability of leukocytes modeled with viscous and elastic structural components," *Physics of Fluids*, vol. 16, no. 2, pp. 244–264, February 2004.

[6] G. Agresar, "A computational environment for the study of circulating cell mechanics and adhesion," Ph.D. dissertation, University of Michigan, 1996.

[7] N. N'dri, "Multi-scale computation in hemodnamics," Ph.D. dissertation, University of Florida, 2002.

[8] G. I. Bell, "Models for the specific adhesion of cells to cells," *Science*, vol. 200, pp. 618–627, 1978.

[9] C. Dong and X. X. Lei, "Biomechanics of cell rolling: shear flow, cell-surface adhesion, and cell deformability," *Journal of Biomechanics*, vol. 33, pp. 35–43, 2000.

[10] E. Evans and B. Kukan, "Passive material behaviour of granulocytes based on large deformation and recovery after deformation tests," *The American Society of Hematology*, vol. 64, pp. 1028–1035, 1984.

[11] R. Tran-Son-Tay, H. P. Ting-Beall, D. Zhelev, and R. Hochmuth, "Viscous behaviour of leukocytes," in *Cell Mechanics and Cellular Engineering*, R. Tran-Son-Tay, H. P. Ting-Beall, D. Zhelev, and R. Hochmuth, Eds., New York, 1994.

[12] A. Yeung and E. Evans, "Cortical shell-liquid core model for passive flow of liquid spheric micropipets," *Biophysical Journal*, vol. 56, pp. 139–149, 1989.

[13] R. M. Hochmuth, H. P. Ting-Beall, B. B. Beaty, D. Needham, and R. Tran-Son-Tay, "Aspiration of human neutrophils: Effects of shear thinning and cortical dissipation," *Biophysical Journal*, vol. 64, pp. 1596–1601, 1993.

[14] D. C. Bottino, "Modeling viscoelastic networks and cell deformation in the context of the immersed boundary method," *Journal of Computational Physics*, vol. 147, pp. 86–113, 1998.

[15] M. Tsai, R. S. Frank, and R. E. Waugh, "Passive mechanical behaviour of human neutrophils: power-law fluid," *Biophysical Journal*, vol. 65, pp. 2078–2088, 1993.

[16] C. Dong and R. Skalak, "Leukocyte-deformability: Finite element modeling of large viscoelastic deformation," *Journal of Theorethicel Biology*, vol. 158, pp. 173–193, 1992.

[17] C. Dong, R. Skalak, and K. L. P. Sung, "Cytoplasmic rheology of passive neutrophils," *Biorheology*, vol. 28, pp. 557–567, 1991.

[18] J. L. Drury and M. Dembo, "Hydrodynamics of micropipette aspiration," *Biophysical Journal*, vol. 76, pp. 110–128, 1999.

[19] ——, "Aspiration of human neutrophils: Effects of shear thinning and cortical dissipation," *Biophysical Journal*, vol. 81, pp. 3166–3177, 2001.

[20] W. Shyy, M. Francois, H. S. Udaykumar, N. N'dri, and R. Tran-Son-Tay, "Moving boundaries in micro-scale biofluid dynamics," *Applied Mechanics Review*, vol. 54, no. 5, pp. 405–453, 2001.

[21] D. E. Ingber, "Cellular tensegrity: Defining new rules of biological design that govern the cytoskeleton." *Journal of Cell Science*, vol. 104, pp. 613–627, 1993.

[22] ——, "Tensegrity i. cell structure and hierarchical systems biology," *Journal of Cell Science*, vol. 116, pp. 1157–1173, 2003.

[23] A. Alshorman, T. David, and P. Walker, "Role of bio-physiochemical parameters in cell adhesion and rolling-simulation analysis," in *ASME Bioengineering Conference*, vol. 50, Leeds, 2001.

[24] P. Bongrand, "Adhesion of cells," *Handbook of Biological Physics*, vol. 1, pp. 755–803, 1995.

[25] D. A. Hammer and M. Tirrell, "Biological adhesion at interfaces," *Annual Review of Materials Science*, vol. 26, pp. 651–691, 1996.

[26] G. I. Bell, M. Dembo, and P. Bongrand, "Cell adhesion. competition between non-specific repulsion and specific bonding," *Biophysical Journal*, vol. 45, pp. 1051–1064, 1984.

[27] E. A. Evans, "Detailed mechanics of membrane-mebrane adhesion and separation.i.continuum of molecular cross-bridges," *Biophysical Journal*, vol. 48, pp. 175–183, 1985.

[28] ——, "Detailed mechanics of membrane-mebrane adhesion and separation.ii.continuum of molecular cross-bridges," *Biophysical Journal*, vol. 48, pp. 185–192, 1985.

[29] D. A. Hammer and D. A. Lauffernburger, "A dynamical model for receptor-mediated cell adhesion to surfaces," *Biophysical Journal*, vol. 52, pp. 475–487, 1987.

[30] C. Cozens-Roberts, D. A. Lauffernburger, and J. A. Quinn, "Receptor-mediated cell attachment and detahment kinetics. i. probabilistic model and analysis," *Biophysical Journal*, vol. 58, pp. 841–856, 1990.

[31] C.Zhu, "Kinetic and mechanics of cell adhesion," *Journal of Biomechanics*, vol. 33, pp. 23–33, 2000.

[32] D. A. Hammer and S. M. Apte, "Simulation of cell rolling and adhesion on surfaces in shear flow: General results and analysis of selectin-mediated neutrophil adhesion," *Biophysical Journal*, vol. 63, pp. 35–57, 1992.

[33] C. Dong, J. Cao, E. Struble, and H. H. Lipowsky, "Mechanics of leukocyte deformation and adhesion to endothelium in shear flow," *Annals of Biomedical Engineering*, vol. 23, pp. 322–331, 1999.

[34] N. N'dri, W. Shyy, R. Tran-Son-Tay, and H. S. Udaykumar, "A multi-scale model for cell adhesion and deformation," in *Proceedings of the ASME conference*, vol. 253, 2000, pp. 205–213.

[35] S. O. Unverdi and G. Tryggvason, "A front tracking method for viscous, incompressible, multi-fluid flows," *Journal of Computational Physics*, vol. 100, pp. 25–37, 1992.

[36] F. H. Harlow and E. Welch, "Numerical calculation of time-dependent viscous incompressible flow of fluids with free surface," *Physics of Fluids*, vol. 8, pp. 2182–2189, 1965.

[37] G. Agresar, J. J. Linderman, G. Tryggvason, and K. G. Powell, "An adaptive, cartesian, front tracking method for the motion, deformation and adhesion of circulating cells," *Journal of Computational Physics*, vol. 143, pp. 346–380, 1998.

[38] R. Peyret and T. D. Taylor, *Computational Methods for Fluid Flow.* Springer-Verlag, 1983.

[39] C. S. Peskin, "Numerical analysis of blood flow in the heart," *Journal of Computational Physics*, vol. 25, pp. 220–252, 1977.

[40] D. N. Needham and R. M. Hochmuth, "A sensitive measure of surface stress in the resting neutrophil," *Biophysical Journal*, vol. 61, pp. 1664–1670, 1992.

[41] R. Tran-Son-Tay, H. P. Ting-Beall, D. Zhelev, and R. Hochmuth, "Human neutrophils under mechnical stress," in *Cell Mechanics and Cellular Engineering*, R. Tran-Son-Tay, H. P. Ting-Beall, D. Zhelev, and R. Hochmuth, Eds., New York, 1994.

[42] D. Needham and R. M. Hochmuth, "Rapid flow of passive neutrophils into a 4 μm pipette and measurement of cytoplasmic viscosity." *Journal of Biomechanical Engineering*, vol. 112, pp. 269–276, 1990.

[43] N. A. N'Dri, W. Shyy, and R. Tran-Son-Tay, "Computational modeling of cell adhesion and movement using a continuum-kinetics approach," *Biophysical Journal*, vol. 85, pp. 2273–2286, 2003.

[44] M. B. Lawrence and T. A. Springer, "Leukocytes roll on a selectin at physiologic flow rates: distinction from and prerequisite for adhesion through integrins," *Cell*, vol. 65, pp. 859–873, 1991.

[45] K.-C. Chang, D. F. J. Tees, and D. A. Hammer, "The state diagram for cell adhesion under flow: Leukocyte rolling and firm adhesion," *Proceedings of the National Academy of Sciences of the United States of America*, vol. 97, pp. 11 262–11 267, 2000.

[46] G. I. Zahalak, W. B. McConnaughey, and E. L. Elson, "Determination of cellular mechanical properties by cell poking, with an application to leukocytes." *Journal of Biomechanical Engineering*, vol. 112, pp. 283–294, 1990.

[47] R. M. Hochmuth, "Mesuring the mechanical properties of individual human blood cells," *Journal of Biomechanical Engineering*, vol. 115, pp. 515–519, 1993.

VITA

Murat Bahadır Soydan was born in Kırklareli, Turkey on April 26, 1979 . He graduated from high school Istanbul Erkek Lisesi in 1998. He received the B. Sc. degree in Mechanical Engineering from Istanbul Technical University (ITU), in 2002. In October 2002, he joined to the Mechanical Engineering Department of Koç University, Istanbul, Turkey as a teaching and research assistant.